Article

Phase Diagram Study of Catanionic Surfactants Using Dissipative Particle Dynamics

Monika Choudhary* and Syed Mohammad Kamil*

Cite This: *ACS Omega* 2022, 7, 29306−29325

Read Online

ACCESS | Metrics & More | Article Recommendations

ABSTRACT: Dissipative particle dynamics (DPD) simulations has been performed to study the phase transition of a mixture of cationic and anionic surfactants in an aqueous solution as a function of the total concentration in water and the relative ratio of surfactants. The impact of the relative difference between the tail lengths of the cationic and anionic surfactants on the phase diagram has been simulated by tuning the number of DPD beads in the simulation model. This research also discusses the impact of the frequently used values of the parameters associated with the harmonic bonds among the bonded DPD beads on the obtained self-assemblies. We find remarkable differences in the resultant self-assemblies based on different choices of harmonic bond parameters. The performed simulations show an enhanced

Density and Stress Profile of a vesicle formed by mixture of cationic and anionic surfactants

spectrum of self-assemblies with augmented tail lengths and disparate harmonic bond parameters. The obtained self-assemblies are quite unique and can potentially be used in the future for various applications. We also compare the simulation results of the vesicle structures obtained by modeling the electrostatic interaction in the simulation among the charged beads by explicitly introducing charges with a long-range interaction with those obtained by tuning the implicit electrostatic interaction without the long-range interaction. The effects of the chain length of the model and the harmonic bond parameters on the internal density of DPD beads and stress profiles within the vesicles are examined closely. These results are a significant contribution to understanding the stability of the phases and tailoring of the desired vesicles.
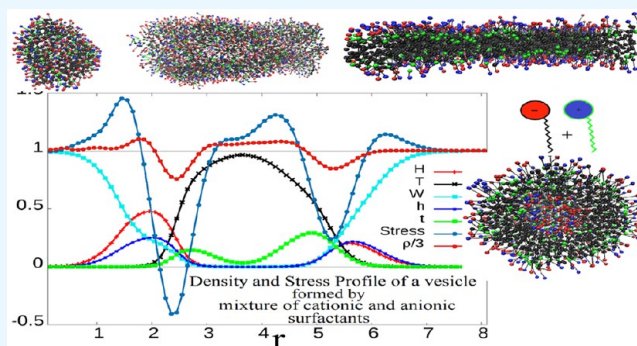
1. INTRODUCTION

Surfactants are amphiphilic molecules that consist of hydrophilic and hydrophobic segments. Surfactant is a portmanteau of surface-active agents due to the high activity on the surfaces. They are frequently used in domestic and industrial applications such as cleaning, hygiene, cosmetics, personal care products, fibers, textiles, paints, plastics, pharmaceuticals, food products, petroleum, and so on. These amphiphilic molecules form various aggregates in aqueous solutions, such as micelles, vesicles, bilayer, and other complex self-assemblies. To further enhance the application of these surfactants, it is necessary to study the factors that modify their phase behavior.[1−5] By changing the various external conditions, the aggregates formed by surfactants can be transformed into one another, such as transforming a micelle into a vesicle.[4] The perpetual dependence on these surfactants makes it much more important to study them thoroughly. There is an abundance of papers on surfactants like sodium dodecyl sulfate (SDS).[6−15] These surfactants have been explored by researchers experimentally as well as computationally. This type of aqueous solution, which is obtained by mixing surfactants of different natures and opposite head charges, is known as a solution of a catanionic surfactant. This terminology was given by Jokela[16] in 1985.

These catanionic surfactants are also called "ion-pair amphiphiles". A close inspection of the studies related to ionic surfactants revealed that mixtures of surfactants with opposite head charges could be of more potential use than a solution that only contains one surfactant in water. In 1985, the term used by Jokela et al. for catanionic surfactant was originally specified for salt-free mixtures only. This division of classes shows a very diverse behavior in the natures of the obtained self-assemblies. This distinctive behavior has been the basis of extensive studies done by various researchers.[17−19]

Catanionic surfactants exhibit interesting properties due to the strong electrostatic attraction between the oppositely charged head groups. This surplus electrostatic potential gives rise to extra flexibility, which further induces the formation of exceptional microstructures that could not be produced in the

solution of a single ionic surfactant.[20,21] Experimentally, it has been confirmed that these mixtures of surfactants with opposite charges have astoundingly low critical aggregation concentrations compared to that of the single surfactant.[20,21] The surface activeness of these surfactants is supposed to be higher than that of the single surfactant.[22,23] Compared to double-chained surfactants, catanionic self-assemblies are very sensitive to temperature, organic additives, and salts.[20] Hence, certain experiments have been performed to understand the micelle-to-vesicle transition in catanionic mixtures under external conditions.[24,25] The sensitivity of catanionic solutions to the external parameters could also be utilized to develop templates for the synthesis of hollow particles and model membranes.[26,27] The micelle-to-vesicle transition could be utilized in micro-reactors and drug delivery.[28−30]

A few researchers have worked on a theoretical continuum-based model to elucidate the various vesicle forms obtained.[31,32] The most commonly used computational technique is molecular dynamics (MD). However, MD has its limitation when it comes to complex fluids due to the associated time and length scales, mainly because of the model interaction potential used between the atoms or molecules. Despite all these constraints, many researchers have performed MD simulations of SDS. A research paper by Shelley et al. based on the MD simulation of SDS was published in 1990.[7] The simulation was run on a 182 ps simulation of a 42 monomer SDS micelle. In 1995, a 120 ps simulation of a 60 monomer SDS micelle was performed.[8] After that, many MD simulation works related to surfactants have been published.[9,10,13,33−35] De Vries et al.[36] reported the MD simulation of vesicle formation in water. However, it was computationally difficult to employ this simulation for large systems due to the limitations of the length and time scales. Similarly, for catanionic mixtures, a molecular dynamics simulation would not be a preferable choice due to the restricted time scale and system size. Considering the above shortcomings of MD, coarse-grain MD could be a boon for the researchers interested in the field of soft matter to study the response or behavior of surfactant self-assemblies or catanionic mixtures. In these simulations, the critical micelle concentration (CMC), density distributions within micelles, and the surface adsorption are calculated using either the MARTINI force field or dissipative particle dynamics.[37−42] The results closely match with both the MD simulation results and the experimental values. In 1993, a solution of catanionic surfactants (SDS and dodecyl trimethylammonium bromide (DTAB) in an aqueous solution) in water was studied experimentally by Herrington et al.[43] A ternary (SDS/DTAB/water) phase diagram was obtained as a result of this research. However, experimental character-ization could not be used to analyze the kinetics of self-assemblies obtained. Thus, it acts as a barrier in the fine assessment of the complex structures obtained so far. Comparatively, theoretical and computational tools have proven to be radical techniques when it comes to microscopic insights.

Dissipative particle dynamics (DPD) is a competent coarse-grained simulation technique that has been broadly used in the field of soft matter physics.[44−52] In DPD, the clusters of atoms within a molecule are replaced by appropriate single units, called beads. These beads are subjected to conservative, dissipative, and random forces as per the model. The time evolution is calculated using Newton's equation of motion. The preference for DPD over other coarse-grained techniques relies on the simplicity and reproducibility of different complex phases in soft matter. The DPD technique was first proposed by Hooger-

brugge and Koelmann in 1992[44] and was first implemented by Groot and Madden in 1998[48] to study a block copolymer. Since then, DPD has been applied to a wide variety of soft matter problems.[53−63] A substantial amount of computational work for self-assemblies has been done in general. However, there are comparatively fewer computational studies specifically based on catanionic mixtures.[58]

In the current research, we explored a catanionic system consisting of cationic and anionic surfactants. We simulated the phase diagrams of self-assemblies of the catanionic mixture as a function of the total concentration in water and the ratio between the cationic and anionic surfactants. We also calculated the effect of tail lengths and harmonic bond parameters on the density and stress profile within a vesicle.

This paper is organized as follows. In section 1, a prologue of the catanionic mixtures is given. Section 2 explains the simulation details, while section 3 provides details of the simulation models. In section 4, a delineation of the simulation results is given. Section 4 contains various subsections explaining the details of the simulation results and discussions of the differences and similarities of the simulation results for the various models. Section V deals with the conclusion and the future perspective.

2. SIMULATION DETAILS

DPD is a coarse-grained simulation technique specifically designed for simulating the hydrodynamic behavior of a polymeric system. DPD is a particle-based technique in which atoms and molecules are lumped (coarse-grained) together as a single entity called DPD-beads. This coarse-graining into DPD-beads is the important feature of this technique, as it plays a major role in increasing the computational speed.[44,45] DPD is similar to MD, but it is possible to analyze complex systems, such as the self-assembly of surfactants, with this technique, which is not feasible with classical methods such as molecular dynamics due to limitations associated with the time and length scales. DPD gives rise to a reduced degree of freedom, hence making the simulation computationally efficient and cheaper compared to others. Thus, it enables the analysis of complex systems at larger time and length scales.

To carry out a DPD simulation, the approach is simple. The primary step is to start with Newton's second law, which is also the first step in molecular dynamics. However, unlike conven-tional molecular dynamics, here the force acting between a pair of DPD beads i and j consists of three components: the conservative force $\vec{F}_{ij}^{C}$, the dissipative force $\vec{F}_{ij}^{D}$, and the random force $\vec{F}_{ij}^{R}$.[47] The total force experienced by the bead i, denoted $\vec{F}_{i}^{DPD}$, can be written as sum of the three forces as mentioned below:

$$\vec{F}_{i}^{DPD} = \sum_{i \neq j} (\vec{F}_{ij}^{C} + \vec{F}_{ij}^{D} + \vec{F}_{ij}^{R})$$

(1)

The forms of these forces are discussed in the following paragraphs.

In the case of ions modeled by DPD beads, and depending on the coarse-graining scheme, $\vec{F}_{ij}^{C}$ can be divided in two parts. One part, $\vec{F}_{ij}^{C_1}$, contains all the short-ranged interactions, and second part, $\vec{F}_{ij}^{e}$, contains the long-ranged explicit electrostatic

Figure 1. Details of coarse-grain models adopted for this study. These models are categorized by the number of DPD beads and the values of the spring parameters (K and r_0; see eq 8). The top line of this figure shows the names of the models. Here M1, M2, M3, M4, and M5 stand for model one, model two, model three, model four, and model five, respectively. The interactions among the beads for these models are shown in Table 1. For every model except cases A and B of model three, i.e., M3 Case:A/B, the cationic surfactant is modeled by two beads. The hydrophobic part is represented by a green bead (tail), the hydrophilic part is represented by a blue bead (head), the head part is represented by h, and the tail part is represented by t. For the anionic surfactant, the surfactants are represented by four, five, or six beads. Red bead represents the hydrophilic head part, which is represented by H, while the black bead represents the hydrophobic tail part, which is represented by T. The value of the spring parameter connecting the beads is shown below each case. For M4 and M5, the charges on the beads are shown by +ve and −ve written beside the beads. M4 has additional counterion beads with charge.

interaction. In this case, the conservative force acting between the beads is given by $\vec{F}_{ij}^{C} = \vec{F}_{ij}^{C_1} + \vec{F}_{ij}^{e}$, where

$$\vec{F}_{ij}^{C_1} = \begin{cases} a_{ij}(1 - r_{ij}/r_c)\hat{r}_{ij} & \text{if } r_{ij} < r_c \\ 0 & \text{if } r_{ij} > r_c \end{cases} \quad (2)$$

and $\vec{F}_{ij}^{e}$ is given by eq 12 and explained in section 3.6.

Typically, to reduce the computational cost, electrostatic interactions are also modeled by tuning the value of a_{ij} to implicitly bring in the effective nature of charge. The terminology adopted for the models used in this study is M1, M2, M3, M4, and M5 where 'M' stands for model and the following value denotes the model number. In this study, we adopted explicit electrostatic interactions in M4 and M5 and implicit electrostatic interactions in the rest of the models. These models are explained in the subsections of section 3. For the beads, which do not contain ions, only $\vec{F}_{ij}^{C_1}$ is used in the models.

$$\vec{F}_{ij}^{D} = -\gamma\omega^{D}(r_{ij})(\hat{r}_{ij}\cdot\vec{v}_{ij})\hat{r}_{ij} \quad (3)$$

$$\vec{F}_{ij}^{R} = \sigma\omega^{R}(r_{ij})\theta_{ij}\Delta t^{-1/2}\hat{r}_{ij} \quad (4)$$

The weight function $\omega^{D}(r_{ij})$ can be chosen arbitrarily but should satisfy the following relations:

$$\omega^{D}(r_{ij}) = [\omega^{R}(r_{ij})]^2 \quad (5)$$

$$\sigma^2 = 2\gamma k_{B}T \quad (6)$$

where k_{B} is the Boltzmann constant. A simple choice for the weight function is given by

$$\omega^{D}(r_{ij}) = \begin{cases} (1 - r_{ij}/r_c)^2 & \text{if } r < r_c \\ 0 & \text{if } r \geq r_c \end{cases} \quad (7)$$

where the prefactor a_{ij} in eq 2 is the maximum repulsive conservative force between the particles i and j, γ is the friction coefficient in the dissipative force, and σ is the noise amplitude in the random force $\vec{F}_{ij}^{R}$. In this paper, we use reduced units only. The mass is given by $m = 1$ for all the DPD beads, and the unit of length is r_c, i.e., the cutoff value. While studying the system, we kept $\sigma = 3$ and $\gamma = 4.5$, which correspond to $k_{B}T = 1$, and the time step Δt was kept at 0.03 τ (τ is the time unit). We used the LAMMPS[64] simulator to integrate Newton's equations of motion using the Shardlow algorithm.[65,66] For bonding between the beads of the surfactant, we used the harmonic spring force given by

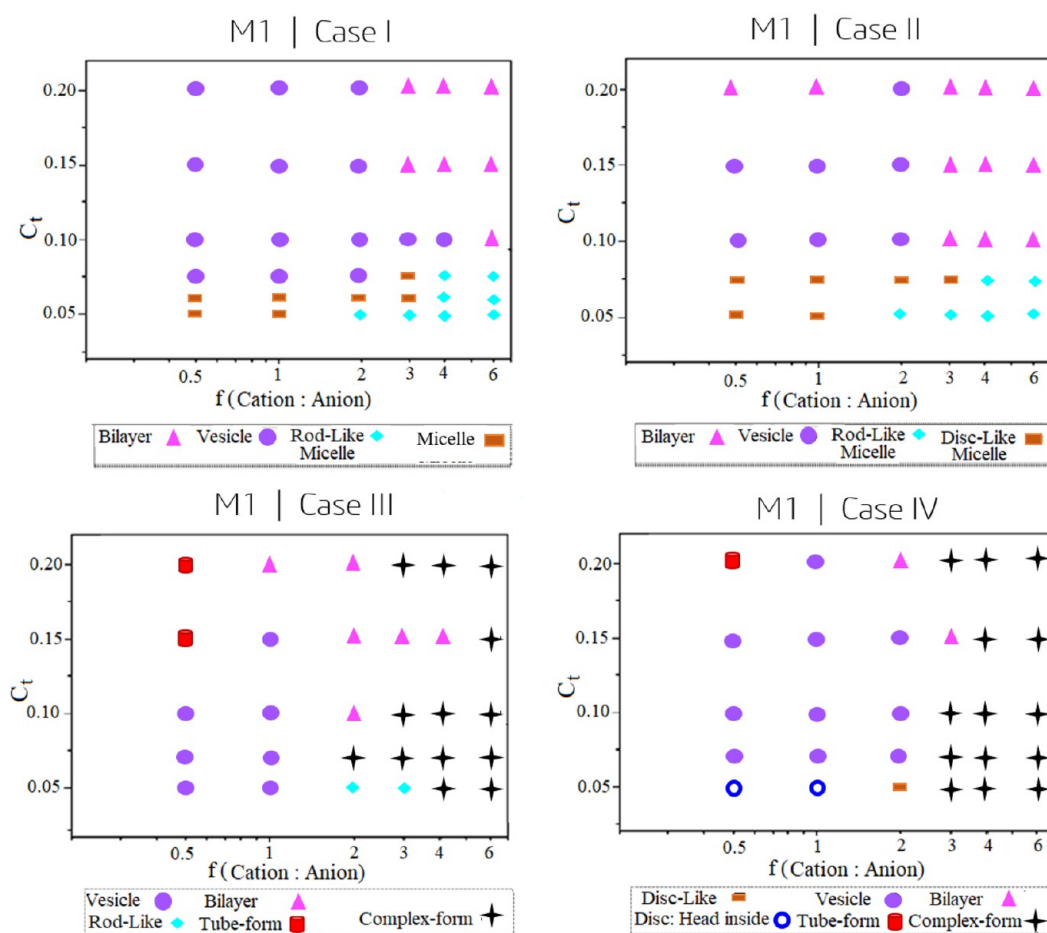$$\vec{F}_{ij} = K(r_{ij} - r_0) \quad (8)$$

Figure 2. Self-assemblies obtained from the DPD simulation for model one (M1) shown in Figure 1. The results of each case are mentioned under the title associated with each name, as explained in section 3 and Figure 1. The ratio of cationic and anionic surfactants is shown along the horizontal axis and is denoted f(Cation:Anion). The total concentration of surfactants in water is shown along the vertical axis and is denoted as C_t. The regions of various self-assemblies are shown by their respective symbols. Indicative images of the micelle, vesicle , and bilayer phases are shown in Figures 6−14.
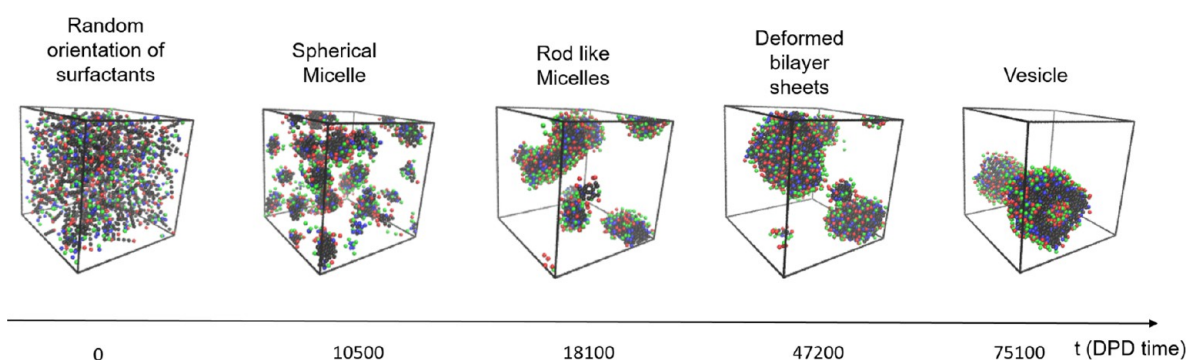

Figure 3. Here we show the kinetics of the evolution of the vesicle phase over time, starting from the random position of surfactants for M1 Case IV. At 7.5×10^4 time steps, the vesicle has already formed. We ran this simulation for 5×10^6 time steps, and the system remained in the vesicle phase. In all Cases, all the calculations on these vesicles were started after at least 5×10^5 steps were run.

where K is spring constant and r_0 is the relaxed length. In literature, different values of the spring constant K and the relaxed length r_0 have been used.[11,12,47,56] However, the most frequent values used are $K = 4$ and $r_0 = 0$ and $K = 100$ and $r_0 = 0.7$, as discussed by Goicochea et al.[56] We performed simulations using both sets of K to understand the difference in the outcomes. The values of a_{ij} are different in the different types of models used in this study, as explained in section 3. In section 3, we also discuss the required details for the chosen

values of a_{ij} in the corresponding model. The size of the simulation box used here is $20 \times 20 \times 20$, and the number density is $\rho = 3$; thus, the box contains 24 000 DPD beads. Periodic boundary conditions and the NVT ensemble were adopted. The effect of the box size on the aggregate structure was investigated. In this work, at least 10^5 DPD steps were skipped at each phase point before any statistical quantity related to the phase behavior was calculated. In Figure 3, we show the kinetics of the evolution of the vesicle phase in time for M1 Case

IV, starting from random position of the surfactants. It is clear from the figure that the vesicle had already formed at 7.5×10^4 time steps. We ran this simulation for 5×10^6 time steps, and system remained in the vesicle phase. We also checked energy and pressure fluctuations to test that the system reached the equilibrium state.[14] These observations clearly indicate that the computation time is long enough for the system to achieve an equilibrium state.

Additionally, it is clear from the calculated values of radii of gyrations, shown in Table 2, that the length of box side is 10 times larger than the size of a surfactant. Hence, we do not expect any finite size effects in the results of our simulation. Despite this, we further performed a simulation for the M1 Case II with box size of $30 \times 30 \times 30$ and a number density $\rho = 3$, containing 81 000 DPD beads, for 10^6 time steps to check the phase stability (see Figure 1) for the total concentration $C_t = 0.1$ and ratio of surfactants $f = 1$ (see Figure 2). The result is depicted in Figure 4 and clearly indicates that the obtained self-assembly is a vesicle (two vesicles of different sizes) only. The simulation results were tested for different initial states.
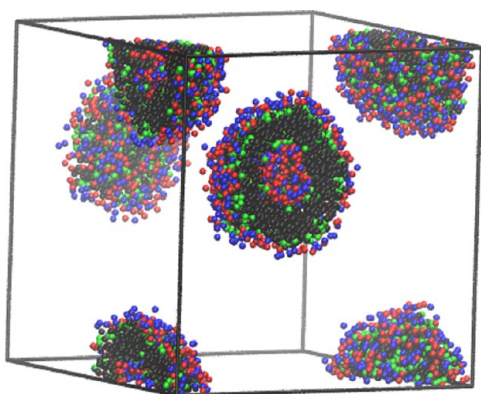

Figure 4. To check the stability of the phase, we performed the simulation for 81 000 particles and a box size of $30 \times 30 \times 30$ for model M1 Case II (see Figure 1) for 10^6 time steps with the total concentration $C_t = 0.1$ and the ratio of surfactants $f = 1$. We still found the vesicle phase, but here we received two different-sized vesicles.

3. CATANIONIC MIXTURE: THE MODEL

The models used in this study are pictorially described in Figure 1. All the models, as shown in Figure 1, describe the mixture of the cationic and anionic surfactants. The names of the models are M1, M2, M3, M4, and M5. The values of the repulsive parameter a_{ij} for DPD interactions among the beads are shown in Table 1. These models were further categorized into several cases depending upon the harmonic bond parameters (K, r_0) given in eq 8 and number of beads involved in the models of the surfactants. Except the M3 Case A/B, the catanionic surfactant is modeled by only two DPD beads, and the anionic surfactant is modeled by four, five, or six DPD beads depending on the category it falls into. Following the publication by Alasiri et al.,[62,67,68] for M3 Case A/B, both types of surfactants in the catanionic mixture are modeled by four beads. In a cationic surfactant, the hydrophobic part is expressed by a green bead (tail), the hydrophilic part is expressed by a blue bead (head), the head part is denoted by h, and the tail part is denoted by t. For anionic surfactants, the red bead indicates the hydrophilic head part, which is represented by H, while the black bead

Table 1. DPD Interaction Parameters a_{ij} from Equation 2 Used In Simulations of the Cationic and Anionic Surfactant Mixture for All Models Shown in Figure 1

M1, M4, and M5	h (cation)	t (cation)	H (anion)	T (anion)	W, W$^+$, or W$^-$
h (cation)	25.0	177.8	25.0	100	25.3
t (cation)	177.8	25.0	100	25.0	151.5
H (anion)	25.0	100	25.0	116.5	25.0
T (anion)	100	25.0	116.5	25.0	75.0
W, W$^+$, or W$^-$	25.3	151.5	25.0	75.0	25.0
M2	h (cation)	t (cation)	H (anion)	T (anion)	W
h (cation)	35.0	177.8	15.0	100	25.3
t (cation)	177.8	25.0	100	25.0	151.5
H (anion)	15.0	100	35.0	116.5	25.0
T (anion)	100	25.0	116.5	25.0	75.0
W	25.3	151.5	25.0	75.0	25.0
M3	h (cation)	t (cation)	H (anion)	T (anion)	W
h (cation)	25.0	43.335	22.0	43.335	23.871
t (cation)	43.335	25.0	60.698	25.0	127.245
H (anion)	22.0	60.698	25.0	60.698	26.078
T (anion)	43.335	25.0	60.698	25.0	127.245
W	23.871	127.245	26.078	127.245	25.0

indicates the hydrophobic tail part, which is represented by T. As discussed previously, the models are further categorized for different values of the spring parameters (K, r_0) connecting the beads, as shown in eq 8. This classification is shown in terms of the case number below every model in Figure 1. In M4 and M5, explicit electrostatic interactions among the charges are implemented, and the charge on the bead is shown by writing +ve or −ve beside the beads. M4 has additional counterions that combine with the water beads to create W$^+$(+ve) or W$^-$(−ve), whereas a neutral water molecule is modeled by a single DPD bead denoted W (neutral).

The motivation for these models is based on papers published at various times for cationic and anionic surfactants.[58,62] In the following subsections, we will focus on the models and the possible interaction parameters involved for each of the models in more detail.

3.1. M1 Case I. In view of their many biological applications,[59−61] mixtures of cationic and anionic surfactants, i.e., catanionic mixtures, have attracted the attention of many researchers.[58,69] Li et al.[58] performed a DPD simulation for catanionic mixtures consists of SDS and DTAB. The objective of their study was to examine the factors responsible for changing a micelle into a vesicle. They developed a DPD model for a SDS and DTAB solution in water and studied the phase behavior and the kinetics of vesicle formation by controlling both the amount of salt and the temperature. In these mixtures, the packing parameter plays a key role.[5] Our study also involves this model (M1 Case I) by Li et al.,[58] all the results of which were reproduced before being subsumed in this research.

In the model given by Li et al.[58] the cationic (DTAB) surfactant was modeled using two beads. One bead forms a hydrophilic part with the chemical formula $-CH_2-N^+(CH_3)_3$, which is represented by h and the second bead forms a hydrophobic part with chemical formula $-C_{11}H_{23}$, which is represented by t. Although DTAB and SDS have carbon chains formed by the same number of carbon atoms, one can see a big difference in their critical micelle concentrations (CMCs). For DTAB, the CMC is 15.6 mM, whereas for SDS it is 8 mM. This difference in the CMC is attributed to the larger size of the head
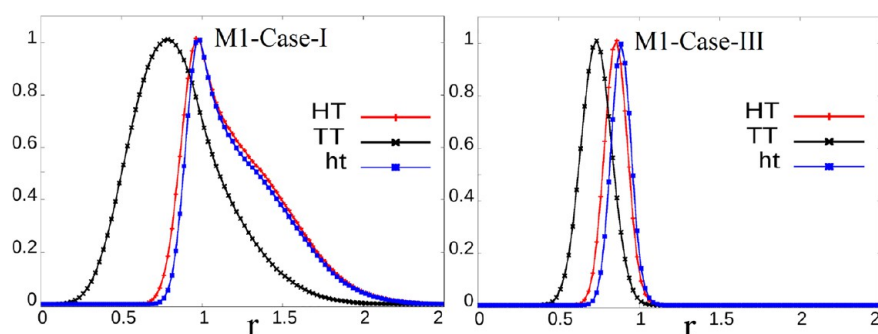
Figure 5. Bond length distributions (BLDs) for M1 Case I and M1 Case III. BLDs for M1 Case II and M1 Case IV are exactly same as those for M1 Case I and M1 Case III, respectively. For other models shown in Figure 1, the distributions for the bonds were found to be similar; hence, their graphs are not shown. The average bond lengths and radii of gyrations for all the models are shown in Table 2.

Table 2[a]

model	L_H	L_T	L_h	L_n	R_A	R_C	$P_{H1}1$	P_{h1}	A_1	P_{H2}	P_{h2}	A_2	$\gamma/3$	p_1	p_2	Δ
M1 Case I	1.23	0.87	1.24	2.02	0.87	0.62	0.43	0.69	0.59	0.33	0.53	0.45	0.596	2.5	5.8	3.3
M1 Case II	1.22	0.88	1.23	2.36	1.00	0.62	0.55	1.06	0.88	0.50	0.96	0.80	0.868	2.0	5.7	3.7
M1 Case III	0.86	0.74	0.89	1.61	0.69	0.45	0.24	0.43	0.34	0.24	0.44	0.35	0.183	3.2	6.0	2.8
M1 Case IV	0.86	0.74	0.89	1.88	0.78	0.44	0.32	0.67	0.50	0.31	0.65	0.49	0.354	2.6	5.9	3.3
M2 Case I	1.21	0.87	1.23	2.00	0.86	0.61	0.38	0.68	0.56	0.36	0.64	0.53	0.81	2.5	5.7	3.2
M2 Case II	1.21	0.88	1.22	2.34	0.96	0.61	0.52	0.99	0.84	0.46	0.88	0.74	0.902	1.9	5.7	3.8
M2 Case III	0.86	0.74	0.89	1.61	0.68	0.45	0.25	0.45	0.35	0.22	0.40	0.32	0.414	3.1	5.7	2.6
M2 Case IV	0.86	0.74	0.89	1.89	0.77	0.45	0.32	0.67	0.52	0.28	0.60	0.46	0.357	2.5	5.6	3.1
M3 Case I	1.13	0.86	1.04	1.88	0.83	0.52	0.38	0.68	0.56	0.36	0.64	0.53	0.640	2.5	5.6	3.1
M3 Case II	1.22	0.87	1.23	2.30	0.96	0.62	0.46	0.86	0.71	0.46	0.86	0.71	0.993	2.1	5.7	3.6
M3 Case III	0.81	0.74	0.78	1.56	0.67	0.39	0.23	0.46	0.34	0.22	0.44	0.33	0.731	3.2	5.8	2.6
M3 Case IV	0.86	0.74	0.89	1.86	0.76	0.44	0.28	0.58	0.45	0.27	0.56	0.43	1.004	2.8	5.7	2.9
M4 Case I	1.22	0.87	1.23	2.00	0.87	0.61	0.45	0.73	0.62	0.41	0.66	0.57	0.702	2.4	5.7	3.3
M4 Case II	1.22	0.88	1.22	2.35	0.99	0.61	0.56	1.09	0.91	0.51	0.99	0.83	1.120	2.0	5.8	3.8
M4 Case III	0.86	0.74	0.89	1.61	0.69	0.45	0.25	0.45	0.36	0.24	0.44	0.36	0.164	3.0	5.8	2.8
M4 Case IV	0.86	0.74	0.89	1.87	0.77	0.45	0.30	0.63	0.49	0.28	0.59	0.46	0.646	2.7	5.7	3.0
M5 Case I	1.20	0.86	1.22	1.98	0.87	0.61	0.43	0.70	0.60	0.42	0.69	0.59	0.823	2.5	5.9	3.4
M5 Case II	1.18	0.86	1.21	2.18	0.91	0.60	0.47	0.86	0.75	0.43	0.78	0.68	0.924	1.9	5.7	3.8
M5 Case III	0.86	0.74	0.89	1.61	0.69	0.45	0.26	0.47	0.37	0.24	0.44	0.35	0.663	3.2	5.9	2.7
M5 Case IV	0.86	0.74	0.89	1.87	0.76	0.45	0.31	0.66	0.51	0.28	0.59	0.45	0.929	2.7	5.8	3.1
M3 Case A	1.25	0.88	1.25	2.10	0.92	0.88	0.49	0.82	0.74	0.44	0.74	0.66	0.279	2.3	5.7	3.4
M3 Case B	0.87	0.74	0.87	1.62	0.70	0.68	0.25	0.47	0.38	0.23	0.43	0.34	1.302	2.9	5.8	2.9
M1 Case II(s)	1.22	0.88	1.23	2.36	0.99	0.62	0.52	0.99	0.82	0.50	0.95	0.79	0.740	1.9	5.7	3.8
M2 Case II(s)	1.20	0.87	1.22	2.28	0.97	0.61	0.50	0.94	0.79	0.48	0.90	0.76	1.140	2.5	5.9	3.4
M3 Case II(s)	1.22	0.87	1.23	2.26	0.95	0.61	0.49	0.90	0.75	0.46	0.84	0.70	1.276	2.7	5.9	3.2
M1 Case VI	0.86	0.74	0.89	2.12	0.86	0.44	0.81	1.96	1.51	0.41	0.99	0.76	−0.271	1.9	5.6	3.7
M2 Case V	1.21	0.88	1.21	2.70	1.08	0.60	2.79	6.22	5.34	0.64	1.43	1.23	1.186	1.3	5.6	4.3
M2 Case VI	0.86	0.74	0.89	2.17	0.87	0.45	0.89	2.16	1.68	0.43	1.04	0.80	−0.094	1.9	5.6	3.7
M5 Case V	1.19	0.86	1.21	2.61	1.07	0.60	1.95	4.22	3.59	0.62	1.35	1.15	1.299	1.6	5.7	4.1
M5 Case VI	0.86	0.74	0.89	2.17	0.87	0.45	0.92	2.26	1.79	0.42	1.03	0.82	−0.049	1.9	5.6	3.7

[a]Here, the bond length averages (BLAs) for the HT bond, the TT bond, and the ht bond and the length of H1Tn are shown in the second (L_H), third (L_T), fourth (L_h), and the fifth (L_n) columns, respectively. The names of the models, described in Figure 1, are shown in the first column. In the sixth (RH) and seventh (R_h) columns, the radii of gyration (RG) are shown for the anionic (H1Tn) and catanionic (ht) surfactants, respectively. According to the scheme described in the text, the calculated packing fractions at the two peaks of the head densities in the vesicle phase are also shown. In the eighth column, P_H^1 stands for the packing fraction for anionic surfactant at the first density peak from the center of the vesicle, as shown in Figures 15−24. Similarly, in the ninth column, P_h^1, refers for the packing fraction for the cationic surfactant at peak one. In the eleventh and twelfth columns, P_H^2 and P_h^2, respectively, refer to the packing fractions at the second peak. In the tenth and thirteenth columns, A_1 and A_2, respectively, refer for the average packing fractions of the mixture, as explained in the text. In the next column, the surface tension (γ) from eq 18 is shown for the models. In the fifteenth, sixteenth, and seventeenth columns, the position of first peak of heads p_1, the position of second peak of heads p_2, and the distance between the two peaks Δ, respectively, are shown.

part of a DTAB molecule, which offers more steric repulsion. Comparatively, due to large size of the head in DTAB, the relative size of the tail in comparison to its head is smaller in DTAB than in SDS. Therefore, this DPD model is adjusted by

controlling the DPD interaction parameter a_{ij} and modeling SDS using four beads, where one bead represents hydrophilic part and the remaining three beads represent the hydrophobic part. The variation between the CMCs of the surfactants in the

cataionic mixture is reflected here by the differences in their tail lengths.[70] This model of SDS is denoted H1T3. Chemically, H represents $-OSO_3$ and T represents $-C_4H_9$.[70] The DPD repulsive interaction parameter, chosen by Li et al.,[58] for the same type of beads (a_{ii}) is 25. This choice was made on the basis of the simulation done by Groot et al. in 1997,[47] which suggested that $a_{ii} = 25$ produces the experimental compressibility of water when the number of water molecules in each DPD bead representing water (N_m) is one. The interaction parameters between different beads were obtained from the work of Chen et al.[55] Chen et al.[55] evaluated the mixing free energy for the two species (SDS and DTAB) via a Monte Carlo simulation and used this value to calculate the Flory−Huggins parameter χ_{ij}.[71] The value of a_{ij} is given by $a_{ij} = a_{ii} + 3.27\chi_{ij}$. Although other schemes are also available for the explicit or implicit inclusion of the electrostatic interactions,[11,12,51,72,73] in this model this effect is not considered. We checked for the effect of the implicit or explicit inclusion of electrostatic interactions in M2 or M4, respectively. For $a_{ii} = 25$, as shown by Goicochea et al.,[56] the first peak of $g(r)$, the radial distribution function (RDF), is around 0.85. Goicochea et al. tested the effect of a_{ii} on the RDF and found that the RDF was mostly unaltered even when the a_{ii} was switched from 25 to 50. The phase diagram presented in the study from Li et al.[58] qualitatively matches the experimental results showed by Herrington et al.[43] Recently, Debashish et al. published the effect of small-angle neutron scattering (SANS) on the aqueous mixture of SDS and DTAB at a total concentration of 50 mM.[74] Except the multilamellar phase, the result of this study also matches the results of the simulations, as shown in Figure 2. However, this model could not capture precipitation in these mixtures, which is a limitation of DPD methods. Moreover, precipitation is generally found only in nearly equimolar compositions or in samples below their Kraft temperature, and even this precipitation can sometimes be blocked, which is described in the Blahnik et al.[75]

Generally, the harmonic interaction acting among the beads, as given in eq 8, is (K, r_0) = (4, 0). However, in the literature, many different sets of values for the harmonic potential parameters are used to incorporate the bonding potential among the bonded beads. Statistically, (K, r_0) = (4, 0) and (K, r_0) = (100, 0.7) are frequently used in DPD simulations.[11,58] These parameters are generally chosen to perpetuate the average distance between the bonded beads. Here, we studied the distribution and the average value of the distance between the beads, and details are shown in Figure 5 and Table 2 for all models. Goicochea et al.[56] also calculated the values for the pressure and surface tension on a plane interface as a function of the spring parameter (K, r_0) and found that the values obtained were essentially the same when using the spring parameter values (K, r_0) = (4, 0) and (K, r_0) = (100, 0.7). Our results, as shown in Figure 5 and Table 2, for the average bond length are also pretty close to these values. In this study, the obtained self-assemblies involve the plane as well as the curved interfaces. Hence, we are interested in the effect of the spring parameter (K, r_0) on the details of a vesicle phase for a given concentration C_t and mixture ratio f(Cation:Anion), as shown in Figure 2. Part of this research work is dedicated to the study of the vesicle phase found at total concentration $C_t = 0.1$ and mixture ratio f(Cation:Anion) = 1.

3.2. M1 Case II and Case V. As shown in Figure 1, in M1 Case II, five DPD beads (H1T4), one head bead (H1) and four tail beads (T4), are used to represent an anionic surfactant, whereas in M1 Case V six DPD beads (H1T5) are used to

represent an anionic surfactant; in both models, the cationic surfactant is modeled by two beads only. the rest of the details of M1 Case II and M1 Case V are same as those of M1 Case I.

For catanionic mixtures, one could assume that the attraction between the heads of the cationic and anionic surfactants is due to their opposite charges causing the surfactants to experience a subtle change in flexibility, which results in various self-assemblies different from the self-assemblies found in the aqueous solution of a single type surfactant. The value of the attraction depends on the condition, namely, whether the salt is present in the catanionic mixture. We studied the effect of the head interactions by comparing the results of the simulations of M2, M4, and M5 with those of M1. However, the majority of changes undergone by these catanionic mixtures could be attributed to the difference in the effective tail lengths of the cationic and anionic surfactants. The variation between the CMCs of the surfactants in the catanionic mixture is reflected in M1 Case I by the difference in their tail lengths.[70] In M1 Case II and M1 Case V, we were interested in studying the impact of tail length and the parameters associated with harmonic bonds between DPD beads on the phase diagram of a catanionic system. Therefore, we add DPD beads representing the tail to the model by Li et al. and modified it in M1 Case II and M1 Case V.

3.3. M1 Case III, Case IV, and Case VI. As shown in Figure 1, in M1 Case III, the anionic surfactant is modeled by H1T3 DPD beads (one head bead, H1, and three tail beads, T3), whereas in M1 Case IV the anionic surfactant is modeled by H1T4 DPD beads (one head bead, H1, and four tail beads, T4); in both cases, the bonded harmonic interaction is (K, r_0) = (100, 0.7). For M1 Case VI, there are six DPD beads for the anionic surfactants (H1T5), and bonded harmonic interaction is (K, r_0) = (100, 0.7). The rest of the details of the models are same as those of M1 Case I.

3.4. M2 Cases I−VI. As we mentioned in section 1, catanionic surfactants exhibit interesting properties due to the strong electrostatic attraction between the oppositely charged head groups.[20,21] This additional electrostatic interaction among the surfactants can be accounted in several ways. One way is to directly model the charge interaction, as suggested by Groot et al. and Gonzalez et al.[72,76] This type of interaction scheme was used in M4 and M5. On the other hand, one could implicitly take this interaction into account by tuning the repulsive parameter a_{ij} among the charged beads, as done by, for example, Mai et al. or Goicochea et al.[11,56] Goicochea et al.[56] used the value of $a_{ij} = 35$ among same charges and the value of $a_{ij} = 15$ among opposite charges. To include the impact of charge in the results, the simulation was performed for many values between 25 and 35 for the repulsive parameter a_{ij} among the heads (H) of anionic surfactants as well as among the cationic surfactant heads (h) and to compensate the attractive interaction between H and h for the values between 15 and 25, and the same phase behavior was found. Hence, we show the result only for $a_{ij} = 35$ and 15 for additional electrostatic repulsion and attraction, respectively, among the charges.

In M2, the repulsive interaction a_{ij} among the heads bearing the same charge increased to 35 from 25 and the value of a_{ij} among beads bearing opposite charges decreased from 25 to 15. The modified interactions are shown in Table 1. As shown in Figure 1, for the anionic surfactant, the H1T3 model (one head bead, H1, and three tail beads, T3) is used in Case I and Case III. Similarly, in Case II and Case IV, the anionic surfactant is modeled by H1T4, while in Case V and Case VI the anionic

surfactant is modeled by H1T5. The harmonic bond with spring parameters $(K, r_0) = (4, 0)$ is used in Case I, Case II, and Case V, while $(K, r_0) = (100, 0.7)$ is used for Case III, Case IV, and Case VI.

3.5. M3 Cases I– IV, Case A, and Case B. For M3, the DPD interactions a_{ij} shown in Table 1 are based on the work by Alasiri et al.[62,67,68] Alasiri et al. used the conductor-like screening model for real solvents (COSMO-RS), a quantum mechanical theory,[77,78] to determine the interaction parameters between the beads as the input for DPD. The interaction parameter between the like beads a_{ii} was chosen to be 25, and that for unlike beads a_{ij} was calculated using the Flory−Huggins parameter χ_{ij}. At first, Alasiri et al.[67,68] calculated the screening charge densities (SCDs) around the molecule and the volumes of the molecules by COSMO calculations using Dmol3. After that, COSMO-RS was used to determine the infinite dilution activity γ_{ij}^{∞} of the solute. They derived eq 9, which connected the parameter χ_{ij}^{∞}, using Flory−Huggins theory, to find γ_{ij}^{∞} and v_{ij}. Here v_{ij} is the ratio of molecular volumes of the solute v_i and v_j.

$$\chi_{ij}^{\infty} = \ln(\gamma_{ij}^{\infty}) + \ln(v_{ij}) - \left(1 - \frac{1}{v_{ij}}\right) \tag{9}$$

Using the relation $\chi_{ij} = 0.286(a_{ij} - a_{ii})$ at $\rho = 3$ and $a_{ii} = 25$ used by Groot and Warren,[47] they determined the value of a_{ij} and found the interfacial tension and CMCs of SDS and DTAB, which were very close to the experimental values. We used the temperature-dependent values of a_{ij} given in the publication by Alasiri et al.[68] at a temperature of 25 °C for SDS and DTAB. The value of the DPD interaction a_{ij} for M3 is shown in Table 1.

They divided both SDS and DTAB into four DPD beads. The tail of the surfactant was modeled by three butyl groups (denoted T3 in Figure 1), and the head was composed of $[\mathrm{SO_4^-Na^+}]$ for SDS (denoted A in Figure 1) and $\mathrm{N(CH_3)_3^+Br^-}]$ for DTAB (denoted C in Figure 1). This model, in our scheme, is denoted M3 Case A and M3 Case B. Spring parameters $(K, r_0) = (4, 0)$ for Case A and $(K, r_0) = (100, 0.7)$ for Case B are used. The details regarding the number of beads for M3 Cases I−IV are same as those explained for M1 and M2 in previous subsections, and the DPD interaction parameter a_{ij} is mentioned in Table 1.

3.6. M4 Cases I−IV. In M4 and M5, we consider the explicit charge interaction between the charged beads. As shown in Figure 1, the charge on the beads is shown by writing +ve or −-ve beside the beads. Following Groot,[72] Gonzalez et al.[76] and Mao et al.,[12] used a smeared charge approach to model electrostatic interactions. As done in this approach, to remove the divergence at the separation $r = 0$ between the charged beads, they considered the charge distribution on DPD particles of the form

$$\rho(r) = \frac{q}{\pi\lambda^3}\exp(-2r/\lambda) \tag{10}$$

where λ is the decay length of the charge, which was chosen as $0.25r_c$ to follow Mao et al.[12] The interaction potential between two charged distributions separated by a distance r from center to center is given by[72]

$$\frac{4\pi u(r)}{\Gamma} = \frac{Z_i Z_j}{r}[1 - (1 + \beta r)\exp(-2\beta r)] \tag{11}$$

where Z_i is the valency of ion i, $\Gamma = e^2/(k_B T \epsilon 0 \epsilon_r r_c)$, e is the electron charge, and $\beta = r_c/\lambda$. From Groot,[72] $\Gamma = 20.08N_m^{1/3}$.

This relation leads to the electrostatic force F_{ij}^e between two charge distributions around charged beads i and j.

$$\frac{4\pi|\vec{F}_{ij}^e|}{\Gamma} = \frac{Z_i Z_j}{r^2}[1 - (1 + 2\beta r(1 + \beta r))\exp(-2\beta r)] \tag{12}$$

We used particle−particle−particle−mesh P^3M to implement the long-range interaction on the periodic boundary condition. The range of the direct interaction in real space was chosen to be $3r_c$. The potential is shown in Figure 19.

The details of the DPD interactions a_{ij} among the beads for M4 and M5 are shown in Table 1. The rest of the details related to number of beads in each case are the same as those explained for M1 in section 3.1. In this model, we consider the counterions of the heads of the surfactants, denoted by W$^+$ and W$^−$, explicitly in Figure 1 and Table 1. In Table 1, we show that the DPD repulsive interaction a_{ij} for W$^+$ and W$^−$ is the same as that of neutral water W, but these beads are subjected to an electrostatic interaction in addition to the DPD repulsive interaction.

3.7. M5 Cases I−Case IV. As we briefly explained in the section 1, one type of catanionic mixtures is salt free. Therefore, in this model, we removed the counterions present in M4 to model salt-free catanionic mixtures. The rest of the details related to the electrostatic interaction and the DPD repulsive interactions are same as those in M4 and are shown in Table 1. The details on the number of DPD beads and the spring parameters (K, r_0) in each case are the same as those from M2 and are explained in section 3.4.

4. RESULTS AND DISCUSSION

First, we start to present the results of the global phase diagram obtained from the simulation of M1 Cases I−IV. Results of the simulations are summarized in Figure 2. The horizontal axis in each Case in Figure 2 shows the ratio of the concentrations of cationic and anionic surfactants and is denoted f(Cation:Anion). The vertical axis shows the total concentration of surfactants in water and is denoted C_t. The self-assemblies of surfactants obtained using these simulations are shown as different symbols, which are defined and displayed below each Case in the subparts of Figure 2. The indicative images of the different self-assemblies are shown in Figures 6−14.

4.1. M1 Case I. The simulation results for Case I are shown in the top left corner of Figure 2. It is clear from the figure that we mainly got four types of self-assemblies, which include the micelles, the rod-like micelle, the vesicle, and the bilayer. The
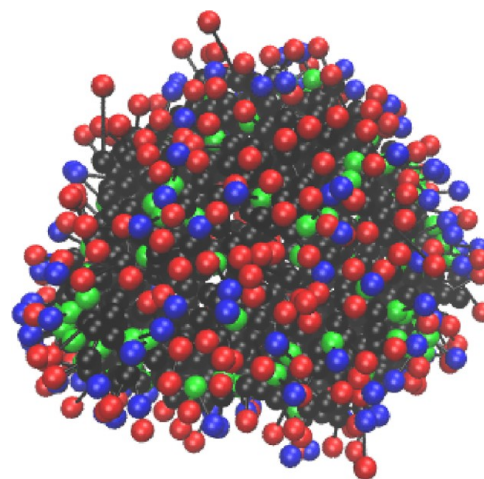

Figure 6. Disk-like micelles obtained as a result of simulating M1 Case II (H1T4 and $K = 4$) (see Figure 1) at $C_t = 0.05$ and $f = 0.5$.
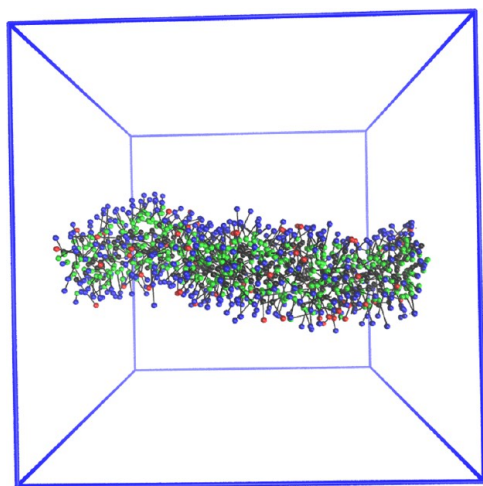
Figure 7. Rod-like micelles obtained as a result simulating M1 Case II (H1T4 and $K = 4$) (see Figure 1) at $C_t = 0.05$ and $f = 6$.
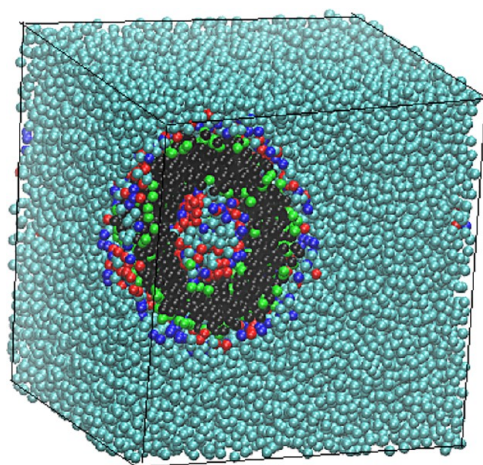

Figure 8. Vesicle obtained as a result of simulating M1 Case II (H1T4 and $K = 4$) (see Figure 1) at $C_t = 0.10$ and $f = 1$ (cross-sectional view).
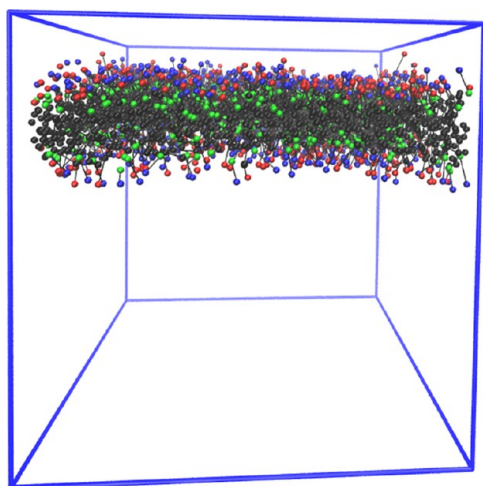

Figure 9. Bilayer phase obtained as a result simulating M1 Case II (H1T4 and $K = 4$) (see Figure 1) at $C_t = 0.20$ and $f = 1$.

Figure 10. Vesicle obtained as a result simulating M1 Case III (H1T3 and $K = 100$) (see Figure 1) at $C_t = 0.05$ and $f = 0.5$.

Figure 11. Tube is obtained as a result of simulating M1 Case III (H1T3 and $K = 100$) (see Figure 1) at $C_t = 0.20$ and $f = 0.5$. This view is a lateral cross section.

aggreement with the results reported by Li et al.[58] We show only the indicative figures of self-assemblies for some cases. As discussed in the follow sections, we also produces these types of self-assemblies in other cases; hence, the number of images shown is optimized.

4.2. M1 Case II. The simulation results for Case II are shown in the top right corner of Figure 2. As mentioned in section 3 and shown in Figure 1, the anionic surfactant chain length in Case II (H1T4) is longer than the anionic surfactant chain length in Case I (H1T3). The types of self-assemblies in Case II are broadly the same as those in Case I, but there are also interesting differences. The shape of the micelles here is more like a disk, as shown in Figure 6. Compared with Case I, for Case II, the region associated with the vesicle phase is smaller and mainly replaced by the bilayer and disk-like micellar phases. By definition, at a low value of f anionic surfactants dominate the solution, whereas at a high value of f cationic surfactants dominate the solution. Since the anionic surfactant chain length is longer in Case II than in Case I, the self-assembly of Case II at the ratio $f = 6$ is the least

micelle phase shown in Case I is not strictly spherical and is closer to disk-like in some cases. We plan to do a detailed study on these in the near future. For Case I, our results are in close
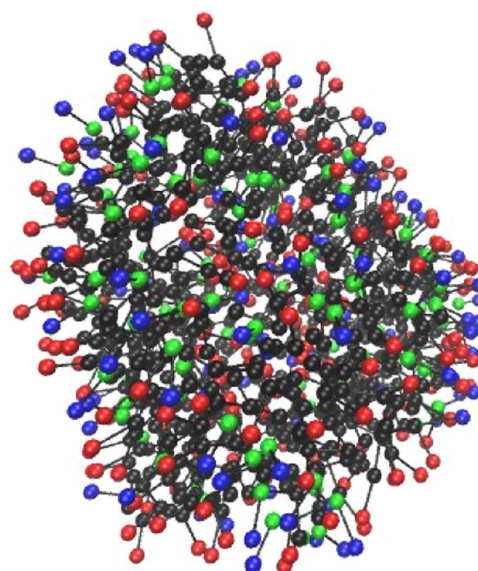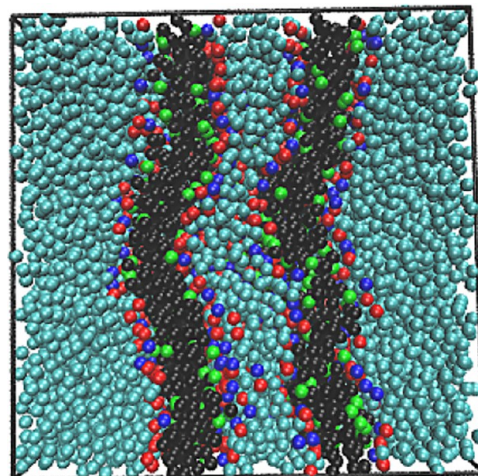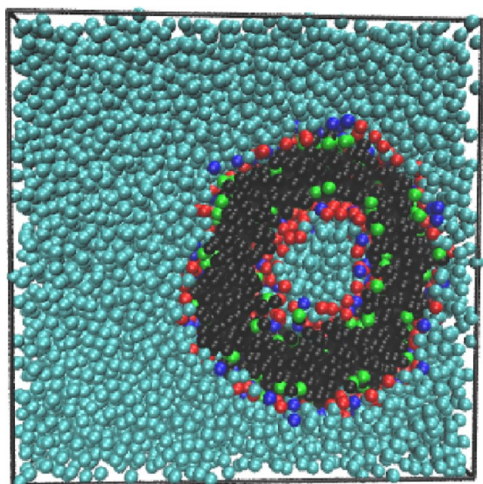
Figure 12. Vesicle is obtained as a result of simulating M1 Case IV (H1T4 and $K = 100$) (see Figure 1) at $C_t = 0.15$ and $f = 0.5$.
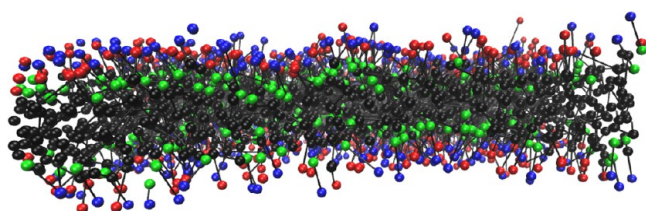

Figure 13. Bilayer obtained as a result of simulating M1 Case IV (H1T4 and $K = 100$) (see Figure 1) at $C_t = 0.20$ and $f = 2$.
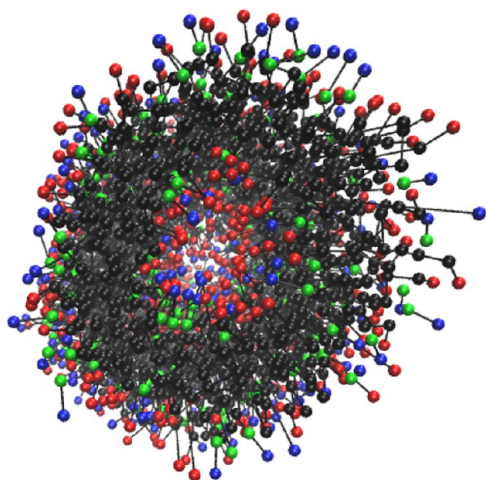

Figure 14. Cross-sectional view perpendicular to the length of a tube obtained as a result of simulating M1 Case IV (H1T4 and $K = 100$) (see Figure 1) at $C_t = 0.20$ and $f = 0.5$.

affected by this chain length increase in the anionic surfactant. Therefore, for all the concentrations, the self-assembly in Case II is the same as that we get in Case I at $f = 6$. In this region, we get a rodlike micelle at low concentrations (C_t) and a bilayer phase at high concentrations (C_t), which is the same scenario as in Case I. The indicative images associated with the rodlike micelle and bilayer phases are shown in Figures 7 and 9 respectively. However, as the value of f decreases, one can notice the differences in the phase diagram of the self-assemblies found in Case II and Case I.

4.3. M1 Case III. The simulation results for M1 Case III are shown in the lower-left corner of Figure 2 below the results of Case I. The model used in Case III varies from the model use in Case I in terms of the spring parameters. As mentioned in section III and shown in Figure 1, in Case III, the value of the spring constant (K) is 100 and the relaxed distance (r_0) is 0.7, whereas in Case I the value of the spring constant (K) is 4 and the relaxed distance (r_0) is 0. As mentioned previously, these values of the spring parameters are commonly used in the literature. The effect of the spring parameter values on the DPD simulation was examined by the Goicochea et al.[56] They explored the effect of the surfactants on the surface tension and pressure of the oil−water planar interface using a DPD simulation. They reported the results of the simulation in the space of the spring parameters (K, r_0). According to their study, the surface tension and pressure have almost same values for the choice of $(K, r_0) = (4, 0.0)$ and $(K, r_0) = (100, 0.7)$. This study by Goicochea et al.[56] was devoted to a flat interface and a low concentration. We were curious whether this state of affairs prevailed in a more general situation. To our surprise, the results for Case III are remarkably different from the results found in Case I, as shown in Figure 2. In Case III, some new types of self-assemblies appeared, which are denoted as tube and complex forms in Figure 2. Indicative images from Case III are shown in the Figures 10 and 11. In Figure 10, we show the indicative image of the vesicle phase. This vesicle phase appeared at $f = 0.5$ and $C_t = 0.05$ for Case III, whereas for Case I it was a micelle phase. In Figure 11, a tube-like structure is shown, which appeared at $f = 0.5$ and $C_t = 0.20$ in Case III. It was not possible to put some of the self-assemblies found in the simulation into simple categories such as vesicle or bilayer. Hence, we give them a combined name of complex self-assemblies. We plan to explore these complex self-assemblies more closely in our future studies.

4.4. M1 Case IV. The simulation results for Case IV (H1T4) are shown in the lower right corner of the Figure 2 below the results for Case II (H1T4). The model used in Case IV differs from the model use in Case II in terms of the spring parameters, as mentioned in section 3 and shown in Figure 1. In Case IV, the value of the spring constant (K) is 100 and the relaxed distance (r_0) is 0.7, which is the same as that in Case III (H1T3), whereas in Cases I (H1T3) and II (H1T4) the value of spring constant (K) is 4 and the relaxed distance (r_0) is 0. The types of self-assemblies obtained in Case IV are broadly the same as those found in Case III. Here we found the tube-like phase, the vesicle phase, the bilayer phase, and the complex phase, which is the same as that in Case III. However, the regions of the various phases in (f, C_t) space are different. The region associated with the bilayer phase of Case III is considerably reduced in favor of other phases in Case IV, as shown in Figure 2. At $C_t = 0.05$ and $f = 2$, we found the disk-like micelle. At small f and low C_t, it seems that the vesicle became oblate in shape. These phases are unique to the Case IV model. We plan to explore these phases in the future. The indicative images of the various phases of Case IV are shown in the Figures 12−14. Comparing the results of Cases III and IV with those of Cases I and III respectively, it is clear that, in contrast to the result of Goicochea et al.,[56] in our case the use of spring parameters $(K, r_0) = (4, 0.0)$ instead of $(K, r_0) = (100, 0.7)$ has a large impact on the phase diagram of the self-assemblies.

The general trend in the phase diagrams discussed above at low concentrations and a ratio of 0.5 is micelle or vesicle. As the ratio f changes from 0.5 to 6, the trend again goes back to rod-like micelles. This is in agreement with the recent experimental
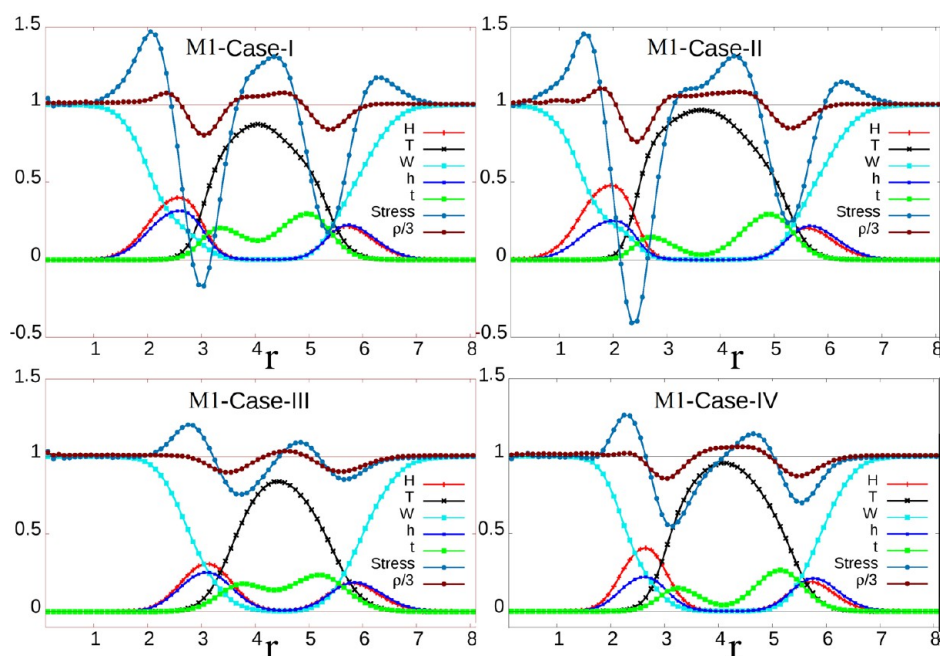
Figure 15. Total density (ρ) and difference in transverse and normal stress ($P_{\text{T}} - P_{\text{N}}$) as a function of distance r from the center of the vesicle for all four cases, i.e., Cases I–IV, at $(f, C_{\text{t}}) = (1, 0.10)$. The legends H and T stand for the relative density of the head and the tail beads of an anionic surfactant respectively, relative to total density ($\rho(r)$). Similarly, the legends h and t stand for the relative densities of the cationic surfactant with respect to the total density ($\rho(r)$). The legend 9W is used to represent the relative density of the water bead with respect to the total density (ρ). In this figure, we plotted $\rho/3$ instead of ρ so that the curve would approach a unit value. In all four cases, it is clear that ρ approaches the value of global density ($\rho_g = 3$) at the center of a vesicle. As we move along the radius of the vesicle, the local value of total density ρ modulates and again smoothly approaches the global density ($\rho_g = 3$) upon reaching outside of the vesicle. Similarly, instead of $P_{\text{N}} - P_{\text{T}}$, we plotted Stress $= \frac{(P_{\text{T}} - P_{\text{N}})}{3} + 1$ to shift the value of stress by one.

results for the SANS data of SDS-DTAB complexes at different SDS-DTAB ratios, as shown by Debashish et al.[74] We can see the types of self-assemblies in detail by going through the phase diagrams in Figure 2. We can also see that at the ratio $f = 1$ the general trend at the low concentration $C_{\text{t}} = 0.1$ is micelle. As we increase the total concentration, the large aggregates that form vesicles to bilayers start to appear, which is in close agreement with experimental result shown by Herrington et al.[43] In all the Cases considered for M1 in our study, one can notice that the vesicle phase is formed at total concentration $C_{\text{t}} = 0.1$ and ratio $f = 1$, as shown in Figure 2. We will see how the details of this vesicle phase change as we introduce changes to our models in the latter sections.

As discussed in section 1, there are various applications of these self-assemblies in almost all industries.[24−27] For example, micelle to vesicle transitions could be utilized in microreactors and drug delivery.[28−30] There could be many important aspects for the study of all the self-assemblies found here, and we should explore them all closely. However, we focus first on the vesicle phase. It is clear from Figure 2 that a vesicle is obtained at $C_{\text{t}} = 0.10$ and $f = 1.0$ in all four Cases. Hence, we chose to focus on $C_{\text{t}} = 0.10$ and $f = 1.0$ in the phase space for a more detailed investigation, and the results of the simulation are presented in the Figures 15−24. In the following subsections, we present the results of the study of the density profiles of the various components that form the vesicle and the profiles of the normal and the transverse stress difference at $(f, C_{\text{t}}) = (1, 0.10)$.

4.5. Packing Fraction. To better understand Figures 15−24, we analyzed the data generated during the simulation, and they are concisely presented in Table 2. In the following lines, we explain the contents of Table 2. The self-assemblies are very sensitive to the packing parameter (P),[5] which is defined as
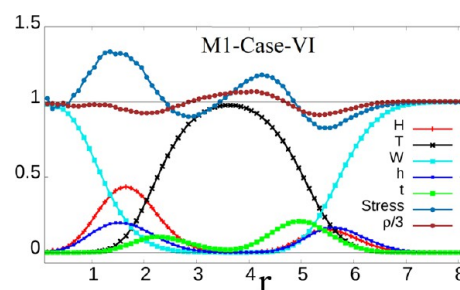

Figure 16. Total density (ρ) and difference in transverse and normal stress ($P_{\text{T}} - P_{\text{N}}$) as a function of distance r from the center of the vesicle for M1 Case VI at $(f, C_{\text{t}}) = (1, 0.10)$. The rest of the details are the same as those mentioned in the caption of Figure 15.

the ratio of the volume (v) of the surfactant molecule to the volume of a cylinder with volume $a_0 l_c$, where a_0 is the projected area of the surfactant head at the interface and l_c is the length of the surfactant molecule.

$$P = \frac{v}{a_0 l_c} \tag{13}$$

The value of P is supposed to be $P \leq 1/3$ for spherical micelles, $1/3 < P < 1/2$ for nonspherical (ellipsoidal) micelles, $P \approx 1/2$ for cylindrical or rod-like micelles, $1/2 < P < 1$ for various interconnected structures, $P \approx 1$ for vesicles and extended bilayers, and finally $P \geq 1$ for a family of "inverted" structures.

For the case of DPD modeling, where the beads are soft and overlap significantly, to performed a packing fraction analysis of DPD, we have to define a parameter that should both depend on the effective size of the DPD-modeled surfactant and the bond
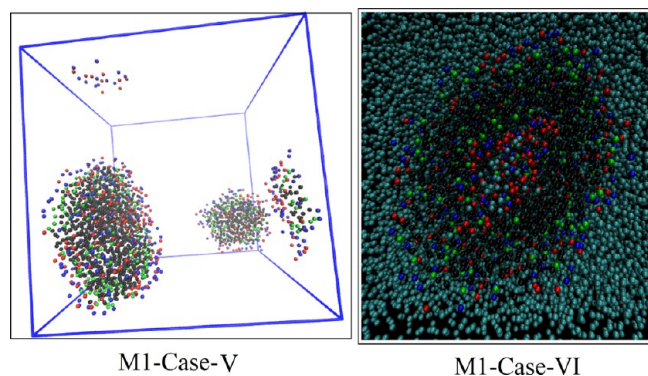
Figure 17. Snapshots of the simulation for M1 Case V (left) and M1 Case VI (right) at the time step of 6×10^5. For M1 Case V, two micelles are formed. One micelle is small, and the other is cylindrical. For M1 Case VI ($K = 100$), the vesicle is formed, but its shape is prolate spheroid and the chains seems to align along the major axis of the spheroid.

lengths and be close to the usual definition of the packing parameter (P), as defined in eq 13.

To determine the various lengths involved in the simulation, we calculated the distribution of the bond lengths for the HT bond, the TT bond, and the ht bond for all the models. One example of such distribution is depicted in Figure 5 for M1 Cases I and III. The bond length distributions for M1 Cases II and IV are exactly same as the results shown in Figure 5; hence, we do not show their distributions separately. For other models shown in Figure 1, the shapes of the distributions are approximately the same as those in Figure 5. We calculated the average of the bond lengths for the HT bond, the TT bond, and the ht bond for all the models, which are shown in second, third, and fourth columns of Table 2 and are denoted L_H, L_T, and L_h, respectively. To calculate the effective or average lengths of the anionic surfactants, we calculated the head-to-tail end distance, which is

shown in the fifth column of Table 2 and denoted L_n. The radii of gyration (RG) for the anionic (R_H) and cationic (R_h) surfactants are shown in the sixth and seventh columns of Table 2, respectively.

It is clear from the density profiles of the vesicles shown in Figure 8 that there are two interfaces (inner and outer) that separate water from the surfactants and form the wall of the vesicle, respectively. Due to their hydrophilic nature, the heads of the surfactants will reside on the two interfaces. If we plot the density profiles of the heads, H and h, of the DPD beads along the radius of the vesicle, the corresponding figure will have two peaks with the densities of the heads at two different positions, as shown in Figure 15. These peak positions, denoted p_1 and p_2, were calculated for all the models from Figure 1, and they are shown in the fifteenth and sixteenth column of Table 2, respectively. The distance between the two peaks, denoted Δ, is shown in seventeenth column of Table 2.

In the following lines, we define parameters P_H^1, P_h^1, P_H^2, and P_h^2 to mimic the packing fractions of the surfactants at the inner and outer interfaces of the wall, separating the water, in a vesicle. We calculated the volumes of the surfactants using the values for the radii of gyrations, R_H and R_h, from the Table 2 for a given model. To calculate the projected area, we calculated the surface area of the interfaces using the interface positions p_1 and p_2 from Table 2 and divided it from the number of total DPD beads N_1 and N_2 at the respective positions. For length l_c, we used the effective lengths L_n and L_h shown in Table 1.

$$P_H^1 = \frac{N_1(R_H)^3}{3(p_1)^2 L_n}, \quad P_h^1 = \frac{N_1(R_h)^3}{3(p_1)^2 L_h} \tag{14}$$

Here N_1 is the number of total DPD beads at peak position p_1.

$$P_H^2 = \frac{N_2(R_H)^3}{3(p_2)^2 L_n}, \quad P_h^2 = \frac{N_2(R_h)^3}{3(p_2)^2 L_h} \tag{15}$$
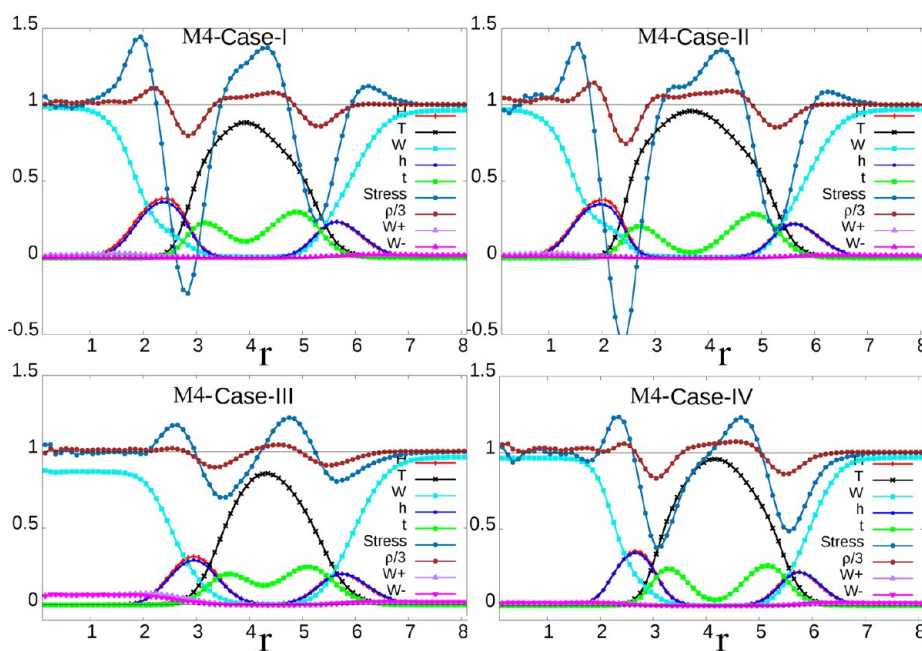

Figure 18. Total density (ρ) and difference in transverse and normal stress ($P_T - P_N$) as a function of distance r from the center of the vesicle for M4 Cases I−IV, at (f, C_t) = (1, 0.10). The counterions are expressed using W+ and W−. The rest of the details are the same as those mentioned in the caption of Figure 15.
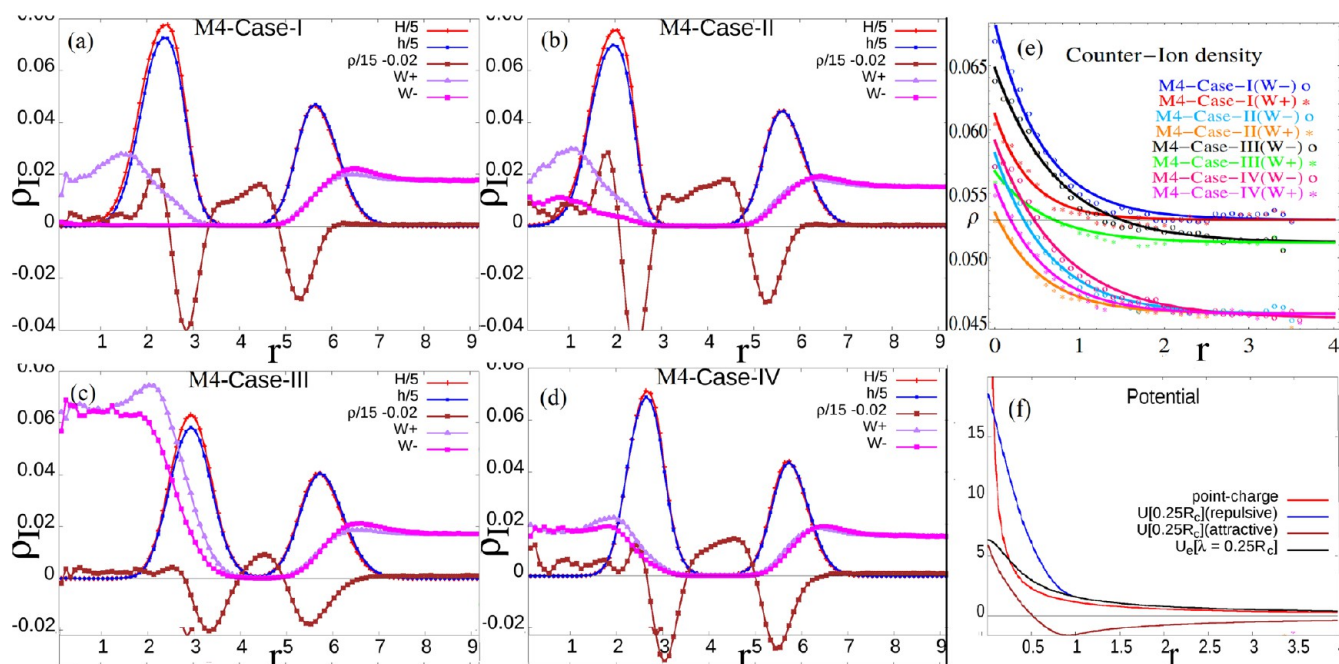
Figure 19. Density of the counterions for for M3. The density of counterions $\rho_I(r)$ is very small compared to the total density $\rho(r)$ shown in Figure 18; hence, to show the details of counterions, the total density ρ and the densities of the anion (H) and the cation(h) are multiplied and displaced as described in the legends of panels a–d. As shown in panels a−c, the counterion density decays very fast and saturates near the second peak of head density of surfactants outside the vesicle. This decay profile is shown in panel e. The profile was further analyzed and fit with $a\exp(-bx) + c$, where x is the distance from the peak position of the counterion density ρ_I. This fit is a good match. The fitting parameters are shown in Table 3. In panel f, the potential action between the beads is shown. In panel f, the red line indicates the electrostatic potential between two point charges of the same sign, $U_e[\lambda R_c]$ shows the smeared charge potential with the decay length $\lambda = 0.25$ (black line). $U[0.25R_c]$(repulsive) and $U[0.25R_c]$(attractive) are the total potential due to the conservative part of the DPD, where $a_{ij} = 25$, and the electrostatic potential determined by the exponentially smeared charge between same charges and opposite charges, respectively.
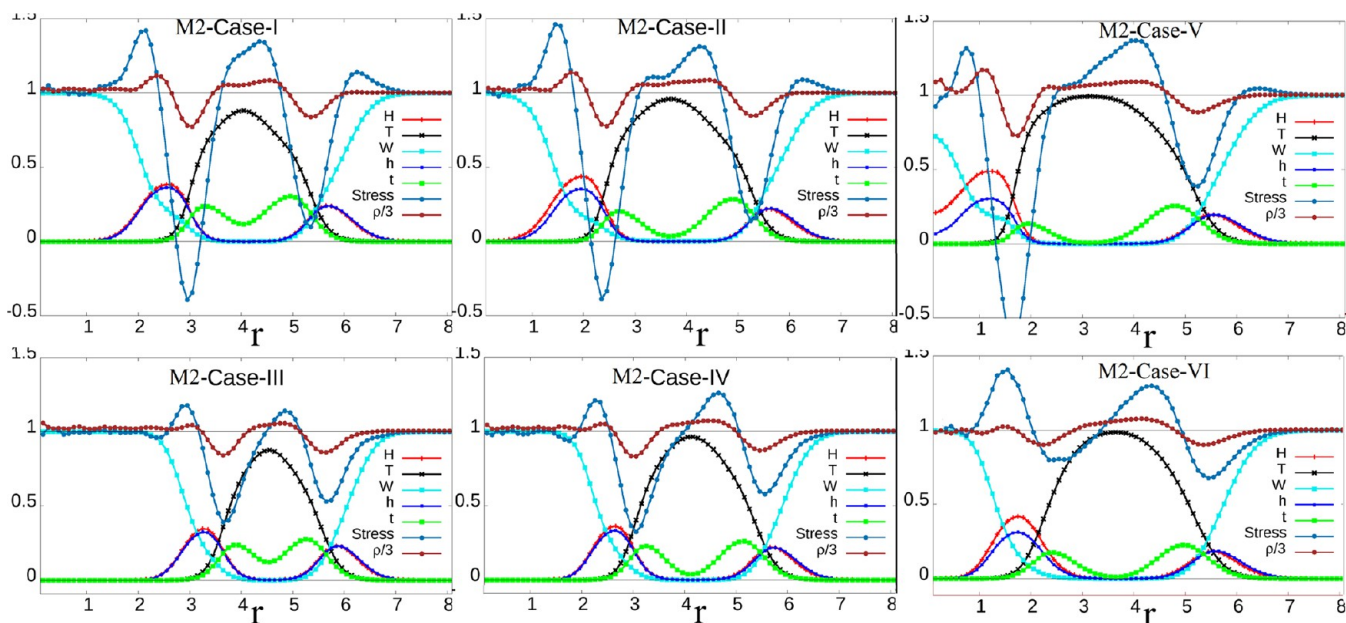

Figure 20. Total density (ρ) and difference in transverse and normal stress $(P_T - P_N)$ as a function of distance r from the center of the vesicle for M5 Cases I−IV at $(f, C_t) = (1, 0.10)$. The rest of the details are the same as those mentioned in the caption of Figure 15.

Here N_2 is the number of total DPD beads at peak position p_2. The values of the packing fractions P_H^1, P_h^1, P_H^2, and P_h^2 for all the models are shown in Table 2. In the tenth and thirteenth columns A_1 and A_2 stand for the average packing fractions of the mixture, which are defined as follows:

$$A_1 = \frac{n_H^1 L_n P_H^1 + n_h^1 L_h P_h^1}{n_H^1 L_n + n_h^1 L_h}, \quad A_2 = \frac{n_H^2 L_n P_H^2 + n_h^2 L_h P_h^2}{n_H^2 L_n + n_h^2 L_h} \quad (16)$$

Here n_H^1, n_h^1, n_H^2, and n_h^2 are the number of DPD head beads for anionic and cationic surfactants at the peak positions p_1 and p_2.
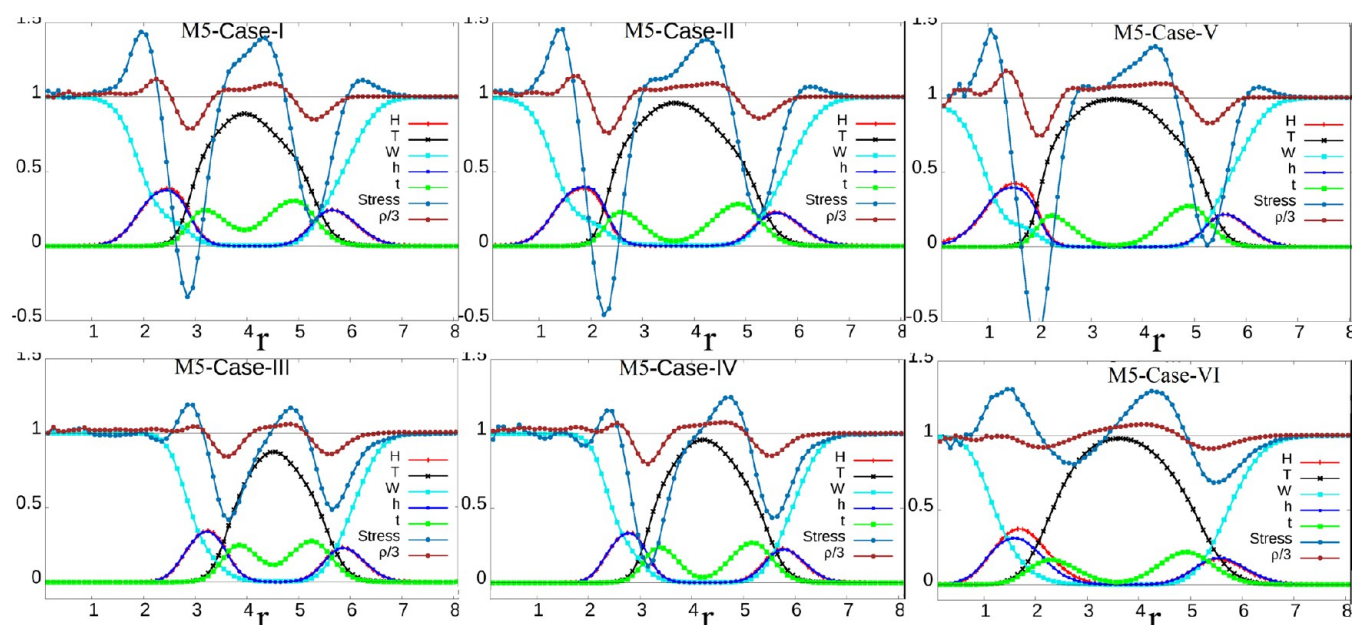
Figure 21. Total density (ρ) and difference in transverse and normal stress ($P_T - P_N$) as a function of distance r from the center of the vesicle for M5 Cases I−IV at $(f, C_t) = (1, 0.10)$. The rest of the details are the same as those mentioned in the caption of Figure 15.

Figure 22. Total density (ρ) and difference in transverse and normal stress ($P_T - P_N$) as a function of distance r from the center of the vesicle for M3 Cases I−IV at $(f, C_t) = (1, 0.10)$. The rest of the details are the same as those mentioned in the caption of Figure 15.
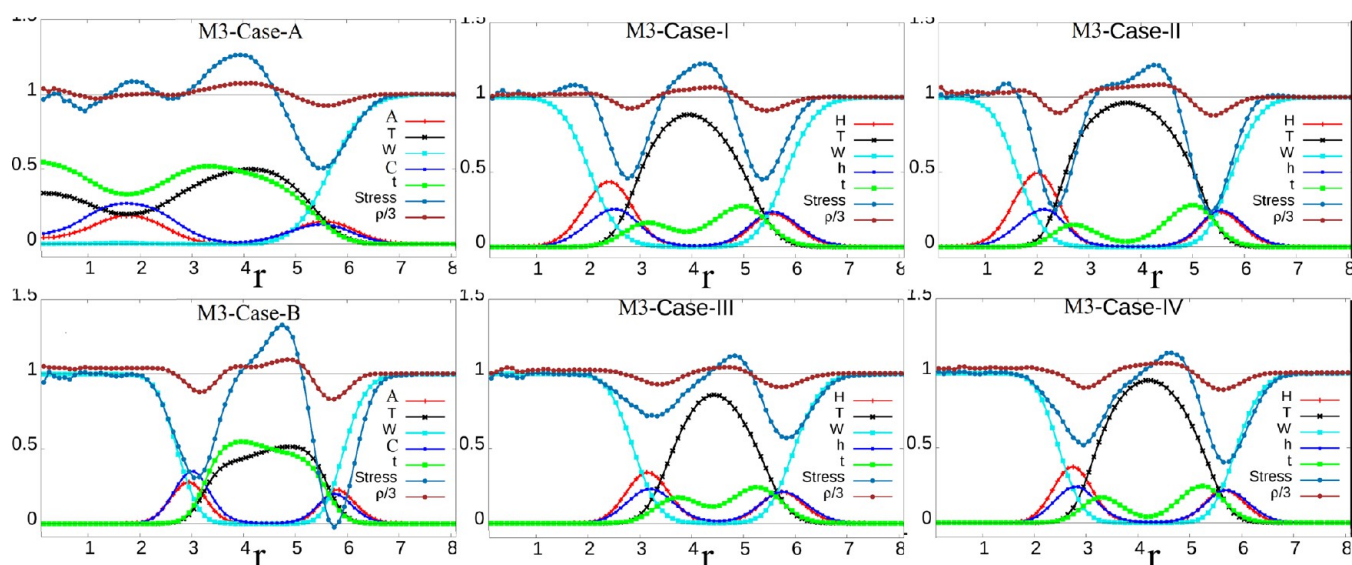
F. Density Profile. In this study, the averaged global density of our system was set as $\rho_g = 3$. As mentioned earlier, the density of DPD beads in the vesicle phase, found in all four cases depicted in Figure 2, was targeted for a close examination. The indicative image of this vesicle is shown in the Figure 12. In Figures 15−24, we plot the local value of the total density $\rho(r)$ of the DPD beads that form the vesicle for all the models depicted in Figure 1 as a function of r, where r is the distance from the center of the vesicle.

To describe the density of beads in the self-assembly, as shown in Figure 15, we take the origin of the spherical coordinates at the center of mass of the vesicle and plot the ratio of the local density of the component bead compared to the total density $\rho(r)$, i.e., the relative density of all components of surfactants and water with respect to $\rho(r)$ along the radius of the vesicle. The color scheme used to represent the various

components of the model is the same as that defined in Figure 1. Hence, in Figure 15, the legends H and T stand for the relative densities of the head and tail beads of an anionic surfactant with respect to the total density $\rho(r)$, respectively. Similarly, the legends h and t stand for the relative densities of the head and tail beads of the cationic surfactant with respect to the total density $\rho(r)$, respectively. The legend W is used to represent the relative density of the water bead with respect to the total density $\rho(r)$. Same procedure was adopted for all the plots in Figures 15−24 showing density profiles.

Similarly, in Figure 18, the relative densities of the counterions in M4, shown in Figure 1, with respect to $\rho(r)$ are represented by W^+ and W^-. Since the counterion density is very small with respect to $\rho(r)$, we further plotted it separately in Figure 19. As discussed in section 3.6, the electrostatic interaction potential is applied explicitly among charged beads in M4 and M5; this
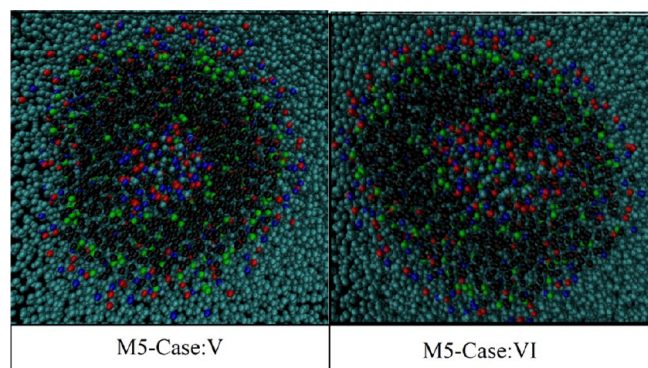
| M5-Case:V | M5-Case:VI |

Figure 23. Snapshots of the simulations of M5 Case V (left) and M5 Case VI (Right) at the time step of 6×10^5. For M5 Case V ($K = 4$), the vesicle is spherical. For M5 Case VI ($K = 100$), the vesicle is formed, but the shape is prolate spheroid and the chains seems to align along the major axis of the spheroid, like the result shown in Figure 17 for M1 Case VI. We found the same behavior for M2 Case V and M2 Case VI, which can also be seen by comparing density and stress profiles from the Figures 20 and 21, respectively.

electrostatic potential is also shown in Figure 19. The densities of the counterions decay very fast and become saturate to a constant value. We fit this value using the function $\rho_I(x) = a\exp(-bx) + c$, where x is the perpendicular distance from the peak position of the counterion density outside the vesicle and a, b, and c are the fitting parameters. This plot is also shown as a subpart of Figure 19, and the best-fitting parameters are shown in Table 3.

4.7. Stress Profile. The Irving–Kirkood method[79,80] is frequently used to calculate surface tension on a planar surface. For example, Goicochea et al.[56] calculated the surface tension γ^* of a binary mixture with a planar interface perpendicular to the z-axis from the components of pressure tensor as follows:

$$\gamma^* = L_z^*\left[\langle P_{zz}^*\rangle - \frac{1}{2}(\langle P_{xx}^*\rangle + \langle P_{yy}^*\rangle)\right] \tag{17}$$

Table 3. Values for the Fitting Parameters in Figure 19e and the Decay of the Counterions in M4[a]

M4	a	b	c
Case I(W+)	0.0082	2.3959	0.0530
Case I(W−)	0.0153	1.7621	0.0530
Case II(W+)	0.0079	1.8056	0.0457
Case II(W−)	0.0125	1.5657	0.0456
Case III(W+)	0.0055	1.6344	0.0512
Case III(W−)	0.0136	1.3660	0.0512
Case IV(W+)	0.0101	1.7099	0.0456
Case IV(W−)	0.0138	1.2755	0.0453

[a]See Figure 1). The decay profile is fit to $\rho_I(x) = a\exp(-bx) + c$, where $\rho_I(x)$ is counterion density at a perpendicular distance x from the surface of the vesicle (see Figure 19e).

where $\langle \cdots \rangle$ is the ensemble average of the pressure tensor $P_{\alpha\alpha}^*$ ($\alpha = x$, y, z) computed from conservative force and the virial theorem. Rowlinson et al.[81] extended this result for spherical surfaces, and the expression in spherical coordinates is as follows:

$$\gamma = \int_0^\infty [\langle P_N(r)\rangle - \langle P_T(r)\rangle]\, dr \tag{18}$$

where $P_N(r)$ and $P_T(r)$ are the normal and transverse components of the stress tensor, respectively.

In the fourteenth column of the Table 2, the surface tension (γ) from eq 18 is shown for all the models shown in Figure 1 at the phase point (f, C_t) = (1, 0.10).

4.8. Analysis of the Simulated Data. To calculate the density profiles $\rho(r)$ shown in the Figures 15−24, we divided the region around the center of mass of the vesicle into spherical shells and calculated the density in that shell. We averaged this result for 10^5 time steps. As we move along the radius of the vesicle, the local value of total density $\rho(r)$ as a function of r changes and smoothly approaches the global density ($\rho_g = 3$) upon reaching the outside of the vesicle. In almost all cases shown in Figures 15−24, we can see that the relative density of
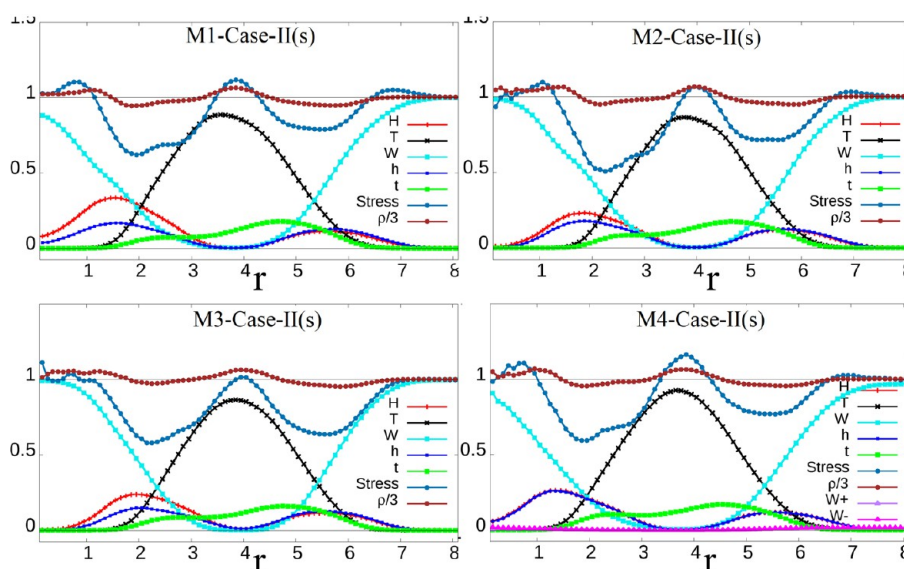
Figure 24. Total density (ρ) and difference in transverse and normal stress ($P_T − P_N$) as a function of distance r from the center of the vesicle for M1 Case II, M2 Case II, M3 Case II, and M4 Case II at (f, C_t) = (1, 0.10). The legend details are same as those explained in the captions of Figures 15 and 22. The profiles, which were simulated for Case II for some initial conditions and did not disappear up to the 10^6 time step, seem to have a stable phase along with the phases shown in Figures 15, 20, 22, and 18.

water (W) reaches 1 at $r = 0$, which shows exclusively water at the center of the vesicle and the absence of all other beads. As we move away from the center $r = 0$ along the radius, we find that the relative density of water (W) decreases from 1.0 and the relative densities of both the cationic head bead (h) and the anionic head bead (H) start to increase from 0. After crossing their respective maxima, H and h both start to decrease. As soon as we go beyond the first peak of H or h toward the outer wall of the vesicle, the relative densities of the cationic tail (t) and the anionic tail (T) start to increase . The relative density of the cationic tail (t) shows two humps in the graphs. Similarly, the relative densities of heads H and h both have two peaks in their graphs, whereas the relative density of the anionic tail (T) has a single peak in its graph. The location of both the peaks of H almost coincide with those of the peaks of h, and their values are shown in Table 2 in the columns fifteen (p_1) and sixteen (p_2). All along the radius where H, h, T, and t marks its presence, the relative density of water W remains low and then increases quickly again to maximum value $W = 1$. Although a considerable number of tail beads are present at the peaks of the heads (p_1 and p_2), the bulk of the tails of the surfactants lie between the peaks of the heads of the surfactants, forming the wall of the vesicle containing the water.

It is clear from the Figures 15−24, that the value of r at which W approaches 1 near the outer surface of the vesicle is almost the same in all models, i.e., the average size of the vesicle is the same. This can also be seen from the position of the second peak of heads (p_2), as shown in Table 2. The value of p_2 is almost constant. As we know, the only difference between the models used for Case I (Case III) and Case II (Case IV) is the number of T beads (See Figure 1), i.e., the tail of an anion is longer by one DPD bead. One can notice from Figures 15−24 and Table 2 that for Case II (Case IV) the first peaks of H and h (p_1) are somewhat shifted toward $r = 0$ in comparison to those for Case I (Case III), while the positions of outer peaks for H and h (p_2) are not affected much. This observation suggests that the amount of water confined in the vesicle for Case II (Case IV) is less than that in Case I (Case III), while the thickness of the wall that forms the vesicle or the distance between the maximum Δ (shown in the last column of Table 2) of the head density is greater for Case II (Case IV) in comparison to Case I (Case III). The same result could be concluded from the observation of the distance between the minima of the total density ρ. The same trend could be noticed by comparing the results of Case I (Case III) with those of Case V (Case VI). After analyzing the results, it was found that adding a bead moved the inner peak position (p_1) approximately $0.6r_c$ toward the center of the vesicle.

To see the effect of the spring parameters, we should compare the results of Case I (Case II) and Case III (Case IV). Recall that the values of the spring parameters (K, r_0) used in Case I (Case II) are given by 4 and 0, respectively, whereas for Case III (Case IV) the values of the spring parameters (K, r_0) are given by 100 and 0.7 (see Figure 1) . As shown by Figures 15−24, for Case I (Case II), the first peaks of H and h are shifted toward $r = 0$ by almost $0.6r_c$ in comparison to Case III (Case IV) while the positions of outer peaks for H and h are not affected much. This observation suggests that the amount of water confined in the vesicle for Case I (Case II) is less than that in Case III (Case IV), and the wall that forms the vesicle is thicker in Case I (Case II) than in Case III (Case IV). The profile of total density $\rho(r)$ for Case I (Case II) is also different from that for Case III (Case IV). The modulation in the total density $\rho(r)$ from $\rho_g = 3$ for Case I (Case II) is more prominent than that for Case III (Case IV).

Unlike the results of Goicochea et al.,[56] these observations show the large impact of the spring parameters (K, r_0) on the density profile. Except for M1, same trend can be seen when comparing the results of Case V (4, 0) and Case VI (100, 0.7). The shape of vesicle for Case VI also changed from spherical to ellipsoidal, as can be seen in Figures 17 and 23. For M1 Case V, the self-assembly is broken into two different micelles, while for M1 Case VI the self-assembly was found to be an ellipsoidal vesicle, as shown in Figure 17. With the shape change from spherical to ellipsoidal, the chains seems to become more parallel, and stiff chains in a parallel arrangement may support a nematic phase such as that in liquid crystals. from M3 Case A (4, 0) to Case B (100, 0.7), the micelle is converted into vesicle, as shown in Figure 22. The density profile for M3 Case A and that for M3 Case B present an interesting case. In this model, it seems that the micelle-to-vesicle transition is not abrupt. The first peak in M3 Case A is shifted toward the outer peak due to change in (K, r_0), and the internal region near the center of the micelle is filled with water, turning the micelle into vesicle.

By analyzing Packing fractions P_H^1, P_h^1, P_H^2, P_h^2, A_1, and A_2 as defined in eqs 14, 15, and 16 and shown in Table 2, it could be noticed that for almost all the cases $P_h^1 > P_H^1$, $P_h^2 > P_H^2$, and $A_1 > A_2$. For a spherical shape, the radius of the curvature at peak one is $1/p_1$ and that at peak 2 is $1/p_2$, but the sign is reversed. The packing fraction for Case II (Case IV) is greater in comparison to that for Case I (Case III), while the packing fraction of Case I (Case II) is greater than that for Case III (Case IV) due to the change in spring parameter values. The same trend could be seen in Case V and Case IV. The major change in the density profile caused by introducing an explicit electrostatic interaction can be noticed in the head profile. When an explicit electrostatic interaction is introduced, the difference between the density of cationic head and that of the anionic head almost disappears (see profiles for M2, M4, and M5). There are differences in the profiles of M4 and M5, which also appear in the packing fraction and the surface tension, but they can not be summarized in a single statement. However, one can see the minute difference in the head profiles of cationic and anionic surfactants. In M1 Case II, for some initial conditions, we find that the equilibrium profile appears in the form shown in Figure 24, which is different from that shown in Figure 15. We simulated this for other models, including M2 Case II, M3 Case II, and M4 Case II, by taking the profile of M1 Case II(s) shown in Figure 24 as initial condition and skipping 10^5 steps. The simulated profiles are plotted in M2 Case II(s), M3 Case II(s), and M4 Case II(s) in Figure 24. The profile seems quite stable across all the models.

As discussed earlier, the effect of the spring parameter values on the DPD simulation was examined by Goicochea et al.[56] In this study, Goicochea et al. explored the effect of surfactants on the surface tension and pressure of an oil−water planar interface using a DPD simulation and reported the results of simulation in the space of the spring parameters (K, r_0). According to their study, the reported results for the surface tension and pressure have almost same values for the choices of (K, r_0) = (4, 0.0) and (K, r_0) = (100, 0.7). As mentioned earlier, we are interested in a more general situation other than a planar interface. Hence, we calculated the expression $[\langle P_N(r) \rangle - \langle P_T(r) \rangle]$ for the vesicles found in all the models shown in Figure 1 at (f, C_t) = (1, 0.10). We calculated the pressure tensor for every DPD bead at every time step. We calculated the position of the center of mass (COM) of the vesicle and divided the region around the COM in 100 spherical shells of thickness 0.1 at every time step. Depending on the position of every bead in the spherical shells,

Table 4. Comparison of the Surface Tension Values ($\gamma/3$) Presented in Column 14 of Table 2[a]

model	Case I	Case II	Case III	Case IV	R21	R43	R13	R24
M1	0.596	0.868	0.183	0.354	1.46	1.93	3.26	2.45
M2	0.810	0.902	0.414	0.357	1.11	0.86	1.55	2.53
M3	0.640	0.993	0.731	1.004	1.55	1.37	0.86	0.99
M4	0.702	1.120	0.164	0.646	1.60	3.94	4.28	1.73
M5	0.823	0.924	0.663	0.929	1.12	1.40	1.24	0.99

[a]Rij stands for the ratio of Case i and Case j.

we calculated the average value of $P_N(r) - P_T(r)$ per bead time and averaged this value for 10^5 time steps. Using symmetry, we can easily convince ourselves that $P_T(r) - P_N(r)$ must be 0 both at the center of a vesicle and outside the vesicle. Hence, the value of $P_T(r) - P_N(r)$ fluctuates about 0. In Figures 15−24, we plotted $\frac{P_T(r) - P_N(r)}{3} + 1$ to match its order with $\rho/3$ to optimize the number of images. The averaged value of $\frac{P_T(r) - P_N(r)}{3} + 1$ is represented by the legend "Stress" in Figures 15−24.

We can easily see from Figures 15−24 that the value of $\left[\frac{\langle P_T(r)\rangle - \langle P_N(r)\rangle}{3} + 1\right]$ is highly correlated with the total density ρ. Since the modulation of the total density $\rho(r)$ from $\rho_g = 3$ in Case II (Case IV) is more than the modulation in Case I (Case II), so too is the value of $\left[\frac{\langle P_T(r)\rangle - \langle P_N(r)\rangle}{3} + 1\right]$. For a better analysis of the effect of the tail length increase and harmonic parameters, we show the ratio of the surface tension (γ) in Table 4. In column number six of Table 4 we depict the ratio of Case II to Case I, which is denoted by **R21**. Similarly, in column number seven the ratio of Case IV to Case III (**R43**) is shown for all the models, from M1 to M5. As shown in Table 4, the value of **R21** for all the models is more than one, which implies that the value of the surface tension increases with the increase in the number of DPD beads in the tail of anionic surfactant for all the models at harmonic parameters $(K, r_0) = (4, 0)$. For harmonic parameters $(K, r_0) = (100, 0.7)$, **R43** similarly shows that the value of surface tension γ increases with the increase in the number of DPD beads in the tail of anionic surfactant for all models except for M2. For M2 this ratio decreases from one, while for M4 this ratio is almost 4 and for M5 this ratio is 1.4. M2 takes the electrostatic interaction in account implicitly by setting the value of parameter a_{ij} to 35 for same charged bead and 15 for charged beads with opposite charges, whereas M4 and M5 account for the electrostatic interaction using explicit charge interactions, as discussed in section 3.6. **R13** shows the ratio of stress at tail length T3 when the harmonic parameters (K, r_0) are changed from $(4, 0)$ to $(100, 0.7)$. Except the M3, the value of **R13** is more than one. The M3 has very different a_{ij} from other models. For M4, this ratio is 4.28. Similarly, **R24** shows the ratio of stress at tail length T4 when the harmonic parameters (K, r_0) are changed from $(4, 0)$ to $(100, 0.7)$. Except for M3 and M5, the ratio **R24** is much larger than 1. This observation suggests that increasing either the tail length of the anionic surfactant or the number of T beads in the model (see Figure 1) supports a larger modulation in the total density ρ and hence a larger variation in Stress, i.e., a larger value for the surface tension γ. Upon comparing the value of Stress, between Case I (Case II) and Case III (Case IV), we find that the choice of spring parameters (K, r_0) between $(4, 0.0)$ and $(100, 0.7)$ has a moderate impact on the surface tension γ. Therefore, we conclude that the surface tension on a curved surface is highly sensitive to the choice of tail length and spring parameters even if the total concentration C_t

and ratio of the surfactants in a catanionic mixture f is same. For all cases, the integration values from eq 18 are shown in Table 2.

V. CONCLUSION AND FUTURE PERSPECTIVE

The simulation results are shown in Figure 2 in the space (f, C_t). We conclude that increasing the tail length while keeping all other factors unchanged produces almost the same type of self-assemblies, but the phase boundaries shift and promote more bilayer and disc-like micellar phases. For example, if Case I (Case III) and Case II (Case IV) are compared, the shift in the phase boundary is evident from the figure itself. For Case II, we can see in Figure 2 that the region of the vesicle phase is smaller as compared to that in Case I and is mainly replaced by bilayer and disc-like micellar phase. Similarly, the types of self-assemblies obtained for Case III and Case IV are more or less the same, but the boundaries are reformed (see Figure 2). For Case IV, some interesting self-assemblies are found around low concentration and close to $f = 0.5$. They appear to be disc-like micelles, which are not found in Case III.

To see how the choice of spring parameters (K, r_0) between $(4, 0)$ and $(100, 0.7)$ (keeping all other factors unchanged) affects the phase diagram, we compared the results of Case I (Case II) and Case III (Case IV), as shown in Figure 2. It is clear from the results of Case I (Case II) and Case III (Case IV) that these two choices create very different phase diagrams in terms of types of self-assemblies and their boundaries. In Case III (Case IV), we find new types of self-assemblies, which were not present in Case I (Case II).

As explained earlier, we examined only the vesicle phase more closely at $(f, C_t) = (1, 0.10)$. In our future work, we plan to explore other types of self-assemblies extensively. To understand the impact of the tail length on the details of the structure of the vesicle, we compared the densities of the DPD beads that form the vesicle and the Stress profiles between Case I (Case III) and Case II (Case IV) in Figures 15−24. We noticed that adding a DPD bead in the anionic surfactant while keeping total concentration same increases the width of the wall by $0.6r_c$ by shifting the inner peak position (p_1) toward the center of the vesicle; however, the overall size of the vesicle remains the same. Adding more DPD beads to the tail and keeping the total concentration the same, the number of available head beads present on the interface separating water and the hydrophobic tail beads decreases. This leads to instability in the vesicle, splitting it into micelles of different sizes, as shown in Figure 17 for the case of M1 Case V. By introducing more attraction among heads, this instability could be controlled. Hence, for M2 Case V and M5 Case V, we see a stable vesicle because of the attractive electrostatic attraction between the oppositely charged heads.

Changing the harmonic bond parameter from $(4, 0)$ to $(100, 0.7)$ causes the vesicle wall to shrink by $0.6r_c$ and become more stiff, leading to a more stable vesicle. However, for rather long chains, the chains become parallel because of their stiffness, and

the shape of the vesicle changes from a sphere to an ellipsoid, as shown for the M2 Case VI and M5 Case VI in Figures 17 and 23, respectively. Explicitly introducing charged DPD beads leads to more attraction among cationic and anionic heads. Hence, the difference between the density profiles of the heads of the anionic H and cationic h surfactants disappears.

We also noticed that the modulation of the total density $\rho(r)$ from $\rho_g = 3$ in Case II (Case IV) is more prominent than the modulation in Case I (Case III), as is the value of the Stress profile. As discussed in the analysis, and shown by the comparison of the surface tension γ in Table 4, this suggests that increasing the tail length of an anionic surfactant or the number of T beads in the model (See Figure 1) supports larger modulations in the total density ρ and a larger variation in Stress, which leads to an increase in the value of the surface tension γ. Similarly, the modulation of the total density $\rho(r)$ from $\rho_g = 3$ in Case I (Case II) is more prominent than the modulation in Case III (Case IV), as is the value of the Stress profile. This observation led us to the conclusion that the stiffness of the bond parameter leads to a reduced value of γ.

Packing fraction-like quantities with a soft interacting potential are defined for the DPD model in eqs 14, 15, and 16. The values of P_H^1, P_h^1, A_1, P_H^2, P_h^2, and A_2 are given in Table 2. In genera,l $P_H^1 < P_h^1$, $P_H^2 < P_h^2$, and $A_1 > A_2$. When a DPD bead is added to the anionic surfactant the packing fraction increases. When the harmonic parameters are changed from $(4, 0)$ to $(100, 0.7)$, the bond lengths (L_T) remain almost the same but the packing fractions $(A_1$ and $A_2)$ decrease. Stress profiles and γ are also highly affected by the change in the harmonic parameters. The observation of $A_1 > A_2$ suggest that the membrane has a natural tendency to spontaneously curve to form a vesicle, which is in line with the theory given by Safran et al.[82]

In the end, we conclude that the type of self-assembly and the surface tension for the curved surface are highly sensitive to the choice of tail length and spring parameters even if the total concentration C_t and the ratio of the surfactants in the catanionic mixture f are kept fixed. These results are very useful for modeling the surfactants with desired qualities and phase behaviors using DPD simulations. It will also help researchers better tailor the surfactant's self-assemblies and provides theorists with a better understanding of the physics of self-assemblies.

AUTHOR INFORMATION

Corresponding Authors

Syed Mohammad Kamil − *Department of Physics, Shiv Nadar University, Greater Noida, Uttar Pradesh 201314, India;* orcid.org/0000-0003-4266-5281; Email: kamil.syed@snu.edu.in, kamilfirst@gmail.com

Monika Choudhary − *Department of Physics, Shiv Nadar University, Greater Noida, Uttar Pradesh 201314, India;* Email: mc805@snu.edu.in

Complete contact information is available at:
https://pubs.acs.org/10.1021/acsomega.2c03507

Notes

The authors declare no competing financial interest.

ACKNOWLEDGMENTS

REFERENCES

(1) Tanford, C. *The Hydrophobic Effect: Formation of Micelles and Biological Membranes,* 2nd ed.; John Wiley & Sons: Somerset, NJ, 1980.

(2) Larson, R. *The Structure and Rheology of Complex Fluids*; Topics in Chemical Engineering; Oxford University Press: New York, NY, 1999.

(3) Schramm, L. L.; Stasiuk, E. N.; Marangoni, D. G. Surfactants and their applications. *Annu. Rep. Prog. Chem., Sect. C Phys. Chem.* 2003, 99, 3−48.

(4) Svenson, S. Controlling surfactant self-assembly. *Curr. Opin. Colloid Interface Sci.* 2004, 9, 201−212.

(5) Israelachvili, J. N. *Intermolecular and Surface Forces,* 2nd ed.; Academic Press: London, England, 1991.

(6) Kékicheff, P.; Grabielle-Madelmont, C.; Ollivon, M. Phase diagram of sodium dodecyl sulfate-water system 1. A calorimetric study. *J. Colloid Interface Sci.* 1989, 131, 112−132.

(7) Shelley, J.; Watanabe, K.; Klein, M. L. Simulation of sodiun dodecyl sulfate. *Int.J.Quatum Mechanics* 1990, 38, 103−117.

(8) MacKerell, A. D. Molecular Dynamics Simulation Analysis of a Sodium Dodecyl Sulfate Micelle in Aqueous Solution Decreased Fluidity of the Micelle Hydrocarbon Interior. *J. Phys. Chem.* 1995, 99, 1846−1855.

(9) Bruce, C. D.; Berkowitz, M. L.; Perera, L.; Forbes, M. D. E. Molecular Dynamics Simulation of Sodium Dodecyl Sulfate Micelle in Water: Micellar Structural Characteristics and Counterion Distribution. *J. Phys. Chem. B* 2002, 106, 3788−3793.

(10) Sammalkorpi, M.; Karttunen, M.; Haataja, M. Structural Properties of Ionic Detergent Aggregates: A Large-Scale Molecular Dynamics Study of Sodium Dodecyl Sulfate. *J. Phys. Chem. B* 2007, 111, 11722−11733. PMID 17877384.

(11) Mai, Z.; Couallier, E.; Rakib, M.; Rousseau, B. Parameterization of a mesoscopic model for the self-assembly of linear sodium alkyl sulfates. *J. Chem. Phys.* 2014, 140, 204902.

(12) Mao, R.; Lee, M.-T.; Vishnyakov, A.; Neimark, A. V. Modeling Aggregation of Ionic Surfactants Using a Smeared Charge Approximation in Dissipative Particle Dynamics Simulations. *J. Phys. Chem. B* 2015, 119, 11673−11683. PMID 26241704.

(13) Zhang, H.; Yuan, S.; Sun, J.; Liu, J.; Li, H.; Du, N.; Hou, W. Molecular dynamics simulation of sodium dodecylsulfate (SDS) bilayers. *J. Colloid Interface Sci.* 2017, 506, 227−235.

(14) Choudhary, M.; Kamil, S. M. Phase Diagram Study of Sodium Dodecyl Sulfate Using Dissipative Particle Dynamics. *ACS Omega* 2020, 5, 22891−22900.

(15) Mitra, S.; Karri, R.; Mylapalli, P. K.; Dey, A. B.; Bhattacharya, G.; Roy, G.; Kamil, S. M.; Dhara, S.; Sinha, S. K.; Ghosh, S. K. Re-entrant direct hexagonal phases in a lyotropic system of surfactant induced by an ionic liquid. *Liq. Cryst.* 2019, 46, 1327−1339.

(16) Khan, A.; Marques, E. Catanionic Surfactants. In *Specialist Surfactants*; Robb, I. D., Ed.; Springer Netherlands: Dordrecht, The Netherlands, 1997; pp 37−80.

(17) Tondre, C.; Caillet, C. Properties of the amphiphilic films in mixed cationic/anionic vesicles: a comprehensive view from a literature analysis. *Adv. Colloid Interface Sci.* 2001, 93, 115−134.

(18) Hao, J.; Hoffmann, H. Self-assembled structures in excess and salt-free catanionic surfactant solutions. *Curr. Opin. Colloid Interface Sci.* 2004, 9, 279−293.

(19) Zemb, T.; Dubois, M.; Deme, B.; Gulik-Krzywicki, T. Self-assembly of flat nanodiscs in salt-free catanionic surfactant solutions. *Science* 1999, 283, 816−819.

(20) Kaler, E. W.; Herrington, K. L.; Murthy, A. K.; Zasadzinski, J. A. N. Phase behavior and structures of mixtures of anionic and cationic surfactants. *J. Phys. Chem.* 1992, 96, 6698−6707.

(21) *Mixed Surfactant Systems,* 2nd ed.; Abe, M., Scamehorn, J., Eds.; CRC Press: Boca Raton, FL, 2004.

(22) Lucassen-Reynders, E.; Lucassen, J.; Giles, D. Surface and bulk properties of mixed anioniccationic surfactant systems i. equilibrium surface tensions. *J. Colloid Interface Sci.* 1981, 81, 150−157.

(23) Kaler, E. W.; Herrington, K. L.; Miller, D. D.; Zasadzinski, J. A. N. Phase Behavior of Aqueous Mixtures of Anionic and Cationic Surfactants Along a Dilution Path. In *Structure and Dynamics of*

Strongly Interacting Colloids and Supramolecular Aggregates in Solution; Chen, S.-H., Huang, J. S., Tartaglia, P., Eds.; Springer Netherlands: Dordrecht, The Netherlands, 1992; pp 571−577.

(24) Bressel, K.; Muthig, M.; Prevost, S.; Gummel, J.; Narayanan, T.; Gradzielski, M. Shaping Vesicles−Controlling Size and Stability by Admixture of Amphiphilic Copolymer. *ACS Nano* **2012**, 6, 5858−5865. PMID 22713309.

(25) Zhang, J.; Liu, S. Kinetics of thermo-induced micelle-to-vesicle transitions in a catanionic surfactant system investigated by stopped-flow temperature jump. *Phys. Chem. Chem. Phys.* **2011**, 13, 12545−12553.

(26) González-Pérez, A.; Castelletto, V.; Hamley, I. W.; Taboada, P. Biomimetic triblock copolymer membranes from aqueous solutions to solid supports. *Soft Matter* **2011**, 7, 1129−1138.

(27) Kępczyński, M.; Lewandowska, J.; Romek, M.; Zapotoczny, S.; Ganachaud, F.; Nowakowska, M. Silicone Nanocapsules Templated Inside the Membranes of Catanionic Vesicles. *Langmuir* **2007**, 23, 7314−7320. PMID 17521201.

(28) Zhao, M.; Yuan, J.; Zheng, L. The formation of vesicles by N-dodecyl-N-methylpyrrolidinium bromide ionic liquidcopper dodecyl sulfate and application in the synthesis of leaflike CuO nanosheets. *Colloid Polym. Sci.* **2012**, 290, 1361−1369.

(29) Jiang, Y.; Luan, Y.; Qin, F.; Zhao, L.; Li, Z. Catanionic vesicles from an amphiphilic prodrug molecule a new concept for drug delivery systems. *RSC Adv.* **2012**, 2, 6905−6912.

(30) Danoff, E. J.; Wang, X.; Tung, S.-H.; Sinkov, N. A.; Kemme, A. M.; Raghavan, S. R.; English, D. S. Surfactant Vesicles for High-Efficiency Capture and Separation of Charged Organic Solutes. *Langmuir* **2007**, 23, 8965−8971. PMID 17658858.

(31) Seifert, U.; Berndl, K.; Lipowsky, R. Shape transformations of vesicles Phase diagram for spontaneous- curvature and bilayer-coupling models. *Phys. Rev. A* **1991**, 44, 1182−1202.

(32) Heinrich, V.; Svetina, S. c. v.; Žekš, B. c. v. Nonaxisymmetric vesicle shapes in a generalized bilayer-couple model and the transition between oblate and prolate axisymmetric shapes. *Phys. Rev. E* **1993**, 48, 3112−3123.

(33) Ryjkina, E.; Kuhn, H.; Rehage, H.; Müller, F.; Peggau, J. Molecular Dynamic Computer Simulations of Phase Behavior of Non-Ionic Surfactants. *Angew. Chem., Int. Ed.* **2002**, 41, 983−986.

(34) Marrink, S. J.; Tieleman, D. P.; Mark, A. E. Molecular Dynamics Simulation of the Kinetics of Spontaneous Micelle Formation. *J. Phys. Chem. B* **2000**, 104, 12165−12173.

(35) Sanders, S. A.; Sammalkorpi, M.; Panagiotopoulos, A. Z. Atomistic Simulations of Micellization of Sodium Hexyl, Heptyl, Octyl, and Nonyl Sulfates. *J. Phys. Chem. B* **2012**, 116, 2430−2437. PMID 22292893.

(36) de Vries, A. H.; Mark, A. E.; Marrink, S. J. Molecular Dynamics Simulation of the Spontaneous Formation of a Small DPPC Vesicle in Water in Atomistic Detail. *J. Am. Chem. Soc.* **2004**, 126, 4488−4489. PMID 15070345.

(37) Marrink, S. J.; Risselada, H. J.; Yefimov, S.; Tieleman, D. P.; de Vries, A. H. Tne MARTINI Force Field: Coarse Grained Model for Biomoleculer Simulation. *J. Phys. Chem. B* **2007**, 111, 7812−7824. PMID: 17569554.

(38) Jalili, S.; Akhavan, M. A coarse-grained molecular dynamics simulation of a sodium dodecyl sulfate micelle in aqueous solution. Colloids and Surfaces A. *Physicochemical and Engineering Aspects* **2009**, 352, 99−102.

(39) Mirjanian, D.; Dickey, A. N.; Hoh, J. H.; Woolf, T. B.; Stevens, M. J. Splaying of Aliphatic Tails Plays a Central Role in Barrier Crossing During Liposome Fusion. *J. Phys. Chem. B* **2010**, 114, 11061−11068. PMID 20701307.

(40) Wang, S.; Larson, R. G. Coarse-Grained Molecular Dynamics Simulation of Self-Assembly and Surface Adsorption of Ionic Surfactants Using an Implicit Water Model. *Langmuir* **2015**, 31, 1262−1271. PMID: 25565113.

(41) Ruiz-Morales, Y.; Romero-Martínez, A. Coarse-Grain Molecular Dynamics Simulations To Investigate the Bulk Viscosity and Critical Micelle Concentration of the Ionic Surfactant Sodium Dodecyl Sulfate (SDS) in Aqueous Solution. *J. Phys. Chem. B* **2018**, 122, 3931−3943. PMID: 29533651.

(42) Alasiri, H. Determining Critical Micelle Concentrations of Surfactants Based on Viscosity Calculations from Coarse-Grained Molecular Dynamics Simulations. *Energy Fuels* **2019**, 33, 2408−2412.

(43) Herrington, K. L.; Kaler, E. W.; Miller, D. D.; Zasadzinski, J. A.; Chiruvolu, S. Phase behavior of aqueous mixtures of dodecyltrimethylammonium bromide (DTAB) and sodium dodecyl sulfate (SDS). *J. Phys. Chem.* **1993**, 97, 13792−13802.

(44) Hoogerbrugge, P. J.; Koelman, J. M. V. A. Simulating Microscopic Hydrodynamic Phenomena with Dissipative Particle Dynamics. *Europhysics Letters (EPL)* **1992**, 19, 155−160.

(45) Koelman, J. M. V. A.; Hoogerbrugge, P. J. Dynamic Simulations of Hard-Sphere Suspensions Under Steady Shear. *Europhysics Letters (EPL)* **1993**, 21, 363−368.

(46) Español, P.; Warren, P. Statistical Mechanics of Dissipative Particle Dynamics. *Europhysics Letters (EPL)* **1995**, 30, 191−196.

(47) Groot, R. D.; Warren, P. B. Dissipative particle dynamics Bridging the gap between atomistic and mesoscopic simulation. *J. Chem. Phys.* **1997**, 107, 4423−4435.

(48) Groot, R. D.; Madden, T. J. Dynamic simulation of diblock copolymer microphase separation. *J. Chem. Phys.* **1998**, 108, 8713−8724.

(49) Groot, R. D. Mesoscopic Simulation of Polymer-Surfactant Aggregation. *Langmuir* **2000**, 16, 7493−7502.

(50) Groot, R.; Rabone, K. Mesoscopic Simulation of Cell Membrane Damage, Morphology Change and Rupture by Nonionic Surfactants. *Biophys. J.* **2001**, 81, 725−736.

(51) Groot, R. D. Applications of Dissipative Particle Dynamics. In *Novel Methods in Soft Matter Simulations*; Karttunen, M., Lukkarinen, A., Vattulainen, I., Eds.; Lecture Notes in Physics, Vol. 640; Springer Berlin Heidelberg: Berlin, Germany, 2004; pp 5−38.

(52) Español, P.; Warren, P. B. Perspective: Dissipative particle dynamics. *J. Chem. Phys.* **2017**, 146, 150901.

(53) Kim, K. Y.; Byun, K.-T.; Kwak, H.-Y. The Mesoscopic Simulation on the Structures of the Surfactant Solution Using Dissipative Particle Dynamics*Proceedings of the ASME 2005 International Mechanical Engineering Congress and Exposition*, Orlando, Florida, November 5−11, 2005; American Society of Mechanical Engineers: New York, NY, 2008; pp 139−144.

(54) Wu, H.; Xu, J.; He, X.; Zhao, Y.; Wen, H. Mesoscopic simulation of self-assembly in surfactant oligomers by dissipative particle dynamics. Colloids and Surfaces A. *Physicochemical and Engineering Aspects* **2006**, 290, 239−246.

(55) Chen, Z.; Cheng, X.; Cui, H.; Cheng, P.; Wang, H. Dissipative particle dynamics simulation of the phase behavior and microstructure of CTABoctane1-butanolwater microemulsion. Colloids and Surfaces A. *Physicochemical and Engineering Aspects* **2007**, 301, 437−443.

(56) Goicochea, A. G.; Romero-Bastida, M.; López-Rendón, R. Dependence of thermodynamic properties of model systems on some dissipative particle dynamics parameters. *Mol. Phys.* **2007**, 105, 2375−2381.

(57) Lee, M.-T.; Vishnyakov, A.; Neimark, A. V. Calculations of Critical Micelle Concentration by Dissipative Particle Dynamics Simulations The Role of Chain Rigidity. *J. Phys. Chem. B* **2013**, 117, 10304−10310. PMID 23837499.

(58) Li, Y.; Zhang, H.; Wang, Z.; Bao, M. Micelle-vesicle transitions in catanionic mixtures of SDSDTAB induced by salt, temperature, and selective solvents a dissipative particle dynamics simulation study. *Colloid Polym. Sci.* **2014**, 292, 2349−2360.

(59) Palivan, C. G.; Goers, R.; Najer, A.; Zhang, X.; Car, A.; Meier, W. Bioinspired polymer vesicles and membranes for biological and medical applications. *Chem. Soc. Rev.* **2016**, 45, 377−411.

(60) Bressel, K.; Gradzielski, M. Enhancing the stability of spontaneously self-assembled vesicles − the effect of polymer architecture. *Soft Matter* **2015**, 11, 2445−2453.

(61) Has, C.; Pan, S. Vesicle formation mechanisms an overview. *J. Liposome Res.* **2021**, 31, 90−111. PMID 32066297.

(62) Alasiri, H. The Behavior of Surfactants in Water Oil System by Dissipative Particle Dynamics. Ph.D. Dissertation, Rice University, Houston, TX, 2016. https://hdl.handle.net/1911/96009.

(63) Ye, X.; Khomami, B. Self-assembly of linear diblock copolymers in selective solvents from single micelles to particles with tri-continuous inner structures. *Soft Matter* **2020**, *16*, 6056−6062.

(64) *LAMMPS Molecular Dynamics Simulator*. http://lammps.sandia.gov.

(65) Larentzos, J. P.; Brennan, J. K.; Moore, J. D.; Lisal, M.; Mattson, W. D. Parallel implementation of isothermal and isoenergetic Dissipative Particle Dynamics using Shardlow-like splitting algorithms. *Comput. Phys. Commun.* **2014**, *185*, 1987−1998.

(66) Lisal, M.; Brennan, J. K.; Avalos, J. B. Dissipative particle dynamics at isothermal, isobaric, isoenergetic, and isoenthalpic conditions using Shardlow-like splitting algorithms. *J. Chem. Phys.* **2011**, *135*, 204105.

(67) Alasiri, H.; Chapman, W. G. Dissipative particle dynamics (DPD) study of the interfacial tension for alkane/water systems by using COSMO-RS to calculate interaction parameters. *J. Mol. Liq.* **2017**, *246*, 131−139.

(68) Alasiri, H. S.; Sultan, A. S.; Chapman, W. G. Effect of Surfactant Headgroup, Salts, and Temperature on Interfacial Properties: Dissipative Particle Dynamics and Experiment for the Water/Octane/Surfactant System. *Energy Fuels* **2019**, *33*, 6678−6688.

(69) Wang, P.; Ma, Y.; Liu, Z.; Yan, Y.; Sun, X.; Zhang, J. Vesicle formation of catanionic mixtures of CTACSDS induced by ratio a coarse-grained molecular dynamic simulation study. *RSC Adv.* **2016**, *6*, 13442−13449.

(70) López-Díaz, D.; Velázquez, M. M. Variation of the Critical Micelle Concentration with Surfactant Structure A Simple Method To Analyze the Role of Attractive-Repulsive Forces on Micellar Association. *Chem. Educator* **2007**, *12* (5), 327−330.

(71) Fried, J. R. *Polymer Science and Technology*, 2nd ed.; Prentice Hall Professional Technical Reference: Upper Saddle River, NJ, 2003.

(72) Groot, R. D. Electrostatic interactions in dissipative particle dynamics—simulation of polyelectrolytes and anionic surfactants. *J. Chem. Phys.* **2003**, *118*, 11265−11277.

(73) Anderson, R. L.; Bray, D. J.; Del Regno, A.; Seaton, M. A.; Ferrante, A. S.; Warren, P. B. Micelle Formation in Alkyl Sulfate Surfactants Using Dissipative Particle Dynamics. *J. Chem. Theory Comput.* **2018**, *14*, 2633−2643. PMID: 29570296.

(74) Saha, D.; Ray, D.; Kumar, S.; Kohlbrecher, J.; Aswal, V. K. Interaction of a bovine serum albumin (BSA) protein with mixed anionic−cationic surfactants and the resultant structure. *Soft Matter* **2021**, *17*, 6972−6984.

(75) Blahnik, J.; Müller, E.; Braun, L.; Denk, P.; Kunz, W. Nanoscopic microheterogeneities or pseudo-phase separations in non-conventional liquids. *Curr. Opin. Colloid Interface Sci.* **2022**, *57*, 101535.

(76) González-Melchor, M.; Mayoral, E.; Velázquez, M. E.; Alejandre, J. Electrostatic interactions in dissipative particle dynamics using the Ewald sums. *J. Chem. Phys.* **2006**, *125*, 224107.

(77) Klamt, A.; Eckert, F. COSMO-RS: a novel and efficient method for the a priori prediction of thermophysical data of liquids. *Fluid Phase Equilib.* **2000**, *172*, 43−72.

(78) Eckert, F.; Klamt, A. Fast solvent screening via quantum chemistry: COSMO-RS approach. *AIChE J.* **2002**, *48*, 369−385.

(79) Irving, J. H.; Kirkwood, J. G. The Statistical Mechanical Theory of Transport Processes. IV. The Equations of Hydrodynamics. *J. Chem. Phys.* **1950**, *18*, 817−829.

(80) Kirkwood, J. G.; Buff, F. P. The Statistical Mechanical Theory of Solutions. I. *J. Chem. Phys.* **1951**, *19*, 774−777.

(81) Rowlinson, J. S.; Widom, B. *Molecular Theory of Capillarity*; Clarendon Press: Oxford, UK, 1982.

(82) Safran, S.; Pincus, P.; Andelman, D. Theory of spontaneous vesicle formation in surfactant mixtures. *Science* **1990**, *248*, 354−356.